

Distributed context-dependent choice information in mouse dorsal-parietal cortex

Javier Orlandi

RIKEN Center for Brain Science

Mohammad Adbolrahmani

RIKEN Center for Brain Science

Ryo Aoki

RIKEN Center for Brain Science

Dmitry Lyamzin

RIKEN Center for Brain Science <https://orcid.org/0000-0002-7082-2902>

Andrea Benucci (✉ andrea@benuccilab.net)

RIKEN Center for Brain Science <https://orcid.org/0000-0002-7698-6289>

Article

Keywords: Decision-making Computations, Mesoscale Activity, Ventral Visual Stream, Recurrent Neural Networks, Context-dependent Dynamics

Posted Date: March 15th, 2021

DOI: <https://doi.org/10.21203/rs.3.rs-288103/v1>

License:   This work is licensed under a Creative Commons Attribution 4.0 International License.

[Read Full License](#)

Distributed context-dependent choice information in mouse dorsal-parietal cortex

Javier Orlandi¹, Mohammad Abdolrahmani¹, Ryo Aoki¹, Dmitry Lyamzin¹, Andrea Benucci^{1,2*}

¹RIKEN Center for Brain Science, 2-1 Hirosawa, Wako-shi, Saitama 351-0198, Japan

²University of Tokyo, Graduate School of Information Science and Technology, Department of Mathematical Informatics, 1-1-1 Yayoi, Bunkyo City, Tokyo 113-0032, Japan

*Corresponding authors: andrea.benucci@riken.jp (A.B)

Abstract

1 Choice information appears in the brain as distributed signals with top-down and bottom-up
2 components that together support decision-making computations. In sensory and associative cortical
3 regions, the presence of choice signals, their strength, and area specificity are known to be elusive and
4 changeable, limiting a cohesive understanding of their computational significance.

5 In this study, examining the mesoscale activity in mouse posterior cortex during a complex visual
6 discrimination task, we found that broadly distributed choice signals defined a decision variable in a low-
7 dimensional embedding space of multi-area activations, particularly along the ventral visual stream. The
8 subspace they defined was near-orthogonal to concurrently represented sensory and motor-related
9 activations, and it was modulated by task difficulty and contextually by the animals' attention state.

10 To mechanistically relate choice representations to decision-making computations, we trained
11 recurrent neural networks with the animals' choices and found an equivalent decision variable whose
12 context-dependent dynamics agreed with that of the neural data.

13 In conclusion, our results demonstrated an independent decision variable broadly represented
14 in the posterior cortex, controlled by task features and cognitive demands. Its dynamics reflected
15 decision computations, possibly linked to context-dependent feedback signals used for probabilistic-
16 inference computations in variable animal-environment interactions.

Introduction

17 Choice signals in the brain reflect a relationship between neural activity and the animal's choice during
18 decision making¹. Previous research has focused particularly on perceptual behaviors, using "choice
19 probability" as a metric to quantify correlations between the activity of neurons and the trial-to-trial
20 fluctuations in animals' choices². The inferred correlations were usually computed by factoring-out task

21 regressors that might inform choices; for instance, a frequently used paradigm is the random-dot
22 discrimination task, used to record from neurons in middle temporal visual area (MT)³. Since in this area
23 neurons clearly encode the direction of stimulus motion, choice probability is measured at near-zero
24 coherence.

25 Choice signals have also been described using a decision variable (DV) derived from neural
26 responses that dynamically followed the decision state of the animal⁴. In evidence accumulation tasks—
27 as the random dots task—the DV is driven by sensory evidence as well as by the animal’s “internal
28 state”, with weak sensory evidence best revealing internally driven computations, such as changes of
29 mind⁵.

30 In posterior cortical regions, choice signals have been characterized by a large degree of
31 heterogeneity^{6–10}. Most studies have focused on individual regions and found that numerous variables
32 can influence the probability of detecting these signals; for instance, the stimulus-coding strength of
33 neurons^{6,11}, the correlation properties of the network^{12,13}, the area location in the sensory hierarchy^{14,15}
34 and even the strategy used by the animal to solve the task¹⁶. Furthermore, choice signals can be difficult
35 to disentangle from coincident task- and behavior-related processes, as those associated with the
36 execution of actions, or with modulatory signals reflecting variability in the attention state of the
37 animal¹⁷. This latter process can contextually enable, route, and gate choice information¹⁸, thus greatly
38 affecting how choice signals are distributed in these areas. It is therefore possible that during a task,
39 choice signals are simultaneously represented across multiple regions, with their magnitude, relative to
40 concurrently represented processes, changing depending on the cortical region, and contextually,
41 according to the variability in the internal state of the animal¹⁹.

42 In this work, we selected a task, recording methodology, and analytical framework that enabled
43 us to examine this possibility. As the animals engaged in a complex variant of a two-alternative forced
44 choice (2AFC) orientation discrimination task²⁰, we performed mesoscale imaging of neural responses
45 (GCaMP) from the mouse posterior cortex. Using recent tensor decomposition methods²¹ and activity-
46 mode analysis²² we isolated choice signals from concurrently represented sensory and motor-related
47 activations, and characterized their distinct spatial and temporal properties across cortical areas. In a
48 reduced space of multi-area activations, choice signals defined an embedding subspace for left or right
49 (L/R) decisions that was near-orthogonal to that of sensory signals and movement components and was
50 modulated by task difficulty. In visual areas, their spatial signature was prominent in ventral stream
51 regions, the areas implicated in the processing of stimulus’ identity. When monitoring fluctuations in the
52 attentional state of the animals, we found that sustained attention differentially modulated the choice
53 signal, but the embedding subspace remained invariant. Modeling the animal behavior with recurrent
54 neural networks (RNNs^{23–25}), trained with the animals’ trial-by-trial decisions, provided mechanistic

55 evidence that the context-dependent representational dynamics reflected the computations underlying
56 the 2AFC task.

Results

57 Mesoscale imaging of dorsal-parietal areas during a discrimination task

58 Using an automated setup featuring voluntary fixation of the animals' heads²⁶ (Fig. 1a), we trained mice
59 ($n = 7$) to carry out a complex version of a 2AFC orientation discrimination task²⁰. The animals had to use
60 their front paws to rotate a toy wheel²⁷ that controlled the horizontal position of two circular grating
61 stimuli presented on a screen positioned in front of them. Each stimulus was presented at monocular
62 eccentricities with orientations that varied from trial to trial. To obtain a water reward, mice had to shift
63 the stimulus most similar to a learned target orientation to the center of the screen (Fig. 1b, c), with the
64 actual learned orientation rarely shown to the animal. Therefore, difficulty had an invariance to absolute
65 orientations, which had to be ignored by the animal, and depended only on the relative orientation
66 between the two stimuli. After reaching performance levels above 75 % correct (Fig. 1d), we used a
67 microscope to image mesoscale GCaMP responses in approximately 12–14 dorsal-parietal cortical areas
68 (Fig. 1e; Methods). In individual trials, the neural activity was highly variable, with response activity
69 associated with the onset of visual stimuli and movements of the limbs, trunk, and eyes, as recently
70 described²⁸ (Fig. 1f).

71 Decomposition of neural responses

72 To extract different variables from the neural signal and map them to defined cortical regions, we
73 adopted a recent variant of non-negative matrix factorization—locaNMF²¹. This decomposition method
74 identifies tensor components associated with specified *seeding* regions. When seeding on a given area,
75 locaNMF decomposes the signal into a sum of separable spatial-temporal tensors, with spatial
76 components constrained by the seeding region and temporal components representing the scaling
77 amplitudes of the spatial components. These temporal vectors are potentially more informative than a
78 single vector computed as the average across spatial locations (pixels) within a given area²¹. We aligned
79 all imaging sessions according to the Allen Common Coordinates Framework (CCF²⁹, Fig. 2a) and seeded
80 the initial spatial decomposition using 10 large regions centered on retinotopically identified areas that
81 extended significantly beyond area boundaries (Extended Data Fig. 1). Consistent with the initial
82 seeding, the factorization typically converged toward components with peak amplitudes within
83 individual retinotopic areas (Fig. 2b). Depending on the seeding region, associated temporal
84 components differentially emphasized sensory or behavioral variables; for instance, when seeding on
85 the primary visual cortex, the largest component (in explained variance, EV) clearly highlighted a

86 stimulus-evoked response (Fig. 2b). However, largest components within parietal regions³⁰ (e.g., A, RL)
87 showed negligible visually driven responses and strong movement-related activations (Fig. 2b). Each
88 locaNMF component provided significant explanatory power, with each main component of a seeding
89 area contributing, on average, 9.6 % of the total explained variance (Extended Data Fig. 1). By contrast,
90 the first PCA component contributed, on average, approximately to 85 % of EV (Extended Data Fig. 1),
91 being strongly influenced by large amplitude movement-related activations³¹. For each area, the
92 proportionality between the surface area and the number of components significantly contributing to
93 the EV (Methods) was not always straightforward; for instance, areas AL and L had commensurate
94 surface area and contributed similarly to the overall EV, but L required about twice as many components
95 as AL (Extended Data Fig. 1). To identify task- and behavior-related variables in locaNMF components,
96 we defined *state* vectors in a multi-dimensional space of component activations (Fig. 2c). This approach
97 further reduced the dimensionality of the data by isolating activity dimensions that linearly
98 discriminated pairs of variables. To examine components associated with visual signals, we defined a
99 stimulus axis as the difference between vectorized tensor components in the presence and absence of
100 the stimulus (Methods). This axis remained stable after the stimulus' appearance (Extended Data Fig. 2)
101 and the projected locaNMF components deviated from the baseline about 200 ms after stimulus onset
102 (Fig. 2d). We quantified the time-dependent increase of detectability of stimulus components using a d'
103 discriminability measure, which can be linked to Fisher information^{32,33}, that bounds the variance for
104 estimating a population-encoded parameter. Different areas contributed to d' with different weights,
105 reaching values greater than one at the peak of stimulus response (Fig. 2d; 1.38 ± 0.13 , mean \pm standard
106 error (s.e)). Using only the LocaNMF components from a particular seeding region allowed us to also
107 quantify the relative contribution of that area to the d' discriminability. For the stimulus variable, the
108 primary and secondary visual cortices (V1, L) had the largest discriminability ($d' = 1.10 \pm 0.09$ and $1.12 \pm$
109 0.13 , respectively), followed by area AL ($d' = 0.51 \pm 0.06$). When attempting to discriminate the
110 orientation of the contra-lateral visual stimulus, no area carried sufficient information, even for the
111 most dissimilar orientation pairs (Extended Data Fig. 3), as expected from the lack of orientation
112 domains in mouse visual cortex³⁴ and the mesoscale spatial resolution of our imaging system.

113 Besides bottom-up visual inputs, imaged dorsal-parietal regions reflected activations associated
114 with general movements of the body and eyes³⁵. Therefore, we defined state axes associated with wheel
115 and eye movements. Projections onto these axes resulted in high discriminability of both types of
116 movements (Fig. 2e, f; peak $d' = 1.29 \pm 0.07$ and 0.94 ± 0.08 for wheel and eye movements,
117 respectively). Area-specific projections highlighted larger contributions by anterior-medial areas (Fig. 2e,
118 f; Extended Data Fig. 2), with d' values increasing before or coincidentally with the detection of

119 movements, suggesting pre-motor contributions (e.g., corollary discharges³⁶), and reaching values
120 greater than one after movement execution.

121 We also identified aspects of the variability in locaNMF components that depended on the
122 attention state of the animal. Underlying changes in sustained attention can be both task-related (e.g.,
123 engagement or motivational state) and task independent components (e.g., arousal or alertness)^{37,38}.
124 Accordingly, in individual sessions we observed fluctuations in performance that correlated with
125 changes in pupil dilations and reaction times (Extended Data Fig. 4)—two biomarkers associated with
126 changes in sustained attention³⁹. Based on the variability in pupil diameter (Methods), we defined a
127 state axis that discriminated between high- and low-attention states (Fig. 2g). Associated d' values
128 deviated significantly from zero largely before stimulus onset (after imposed zero discriminability at trial
129 onset; see Methods). Discriminability values reached $d' = 0.5$ approximately 0.5 s after trial onset and
130 remained above this value throughout the trial duration, with peak $d' = 1.31 \pm 0.09$. The state axis
131 defined by attentional modulations remained stable throughout the duration of the trial (Extended Data
132 Fig. 2), consistent with periods of high and low attention that persisted across trials³⁵. The anterior-
133 medial visual areas and the retrosplenial cortex contributed most significantly to large d' discriminability
134 (Fig. 2g, Extended Data Fig. 2).

135 Together, these results showed that sensory inputs, movement-related activations, and
136 attentional signals were concurrently present in the dorsal-parietal regions, and could be separated by
137 the locaNMF tensor decomposition, permitting the identification of their characteristic spatial and
138 temporal signatures.

Choice signals

139 This approach also allowed us to identify choice-related signals. We adopted a broad operational
140 definition of “choice” as signals that correlated with animal’s L/R decisions, independently of the
141 stimulus and with premotor signatures reflecting action-selection⁹. We considered trials in which the
142 first detected wheel rotation occurred at least half a second after stimulus onset. The first detected
143 movement after stimulus presentation did not always coincide—by definition—with the movement
144 signaling the animal’s choice, which occurred in the closed-loop (CL, Methods) period and terminated
145 the trial. However, we confirmed that the direction of the first movement had a large and significant
146 correlation with the final choice (85 ± 4 % agreement with movement directions), suggesting that the
147 decision was made quickly after the stimulus presentation (Extended Data Fig. 4, 5). We then aligned
148 responses relative to movement times and defined a state axis that linearly discriminated clockwise
149 from counterclockwise wheel rotations (hereafter left and right choice, respectively). LocaNMF
150 projections onto this axis sharply separated left from right choices (Fig. 3a), reaching peak separation

151 values approximately 0.15 s after movement detection (Fig. 3b; peak $d' = 1.5 \pm 0.1$), and with the choice
152 axis showing two clearly stable regions, before and after movement onset (Fig. 3c). Global and area-
153 specific d' values started to increase before movement onset (Fig. 3d). We characterized pre-movement
154 components using a piecewise linear regression analysis (Fig. 3e) applied to d' curves to quantify the
155 slope of the fit before the movement and the time of the slope change (Fig. 3f, g; slope = 0.19 ± 0.06
156 d'/s , time of slope change = -0.06 ± 0.02 s). We found a consistent trend for positive pre-movement
157 slopes (ramping) and pre-movement slope change times, providing evidence for distributed pre-
158 movement choice components across these regions.

159 We reasoned that, although evidence accumulation might not be a significant factor in our task,
160 a decision variable⁴⁰—reflected in the time-varying d' values—would still retain its sensitivity to task
161 difficulty. Indeed, we found that in high-attention states, d' curves reflected stronger choice separation
162 in easy trials than in difficult trials (Fig. 3h; peak $d' = 1.4 \pm 0.1$ and 1.3 ± 0.1 , respectively; paired t-test, p
163 = 0.003). In low-attention states, there was a similar trend, but the difference was not significant (paired
164 t-test, $p = 0.4$). The dependence of d' values on task difficulty in high-attention states revealed a
165 modulatory effect of attention on choice signals. However, when we analyzed the average separation
166 between trajectories across attention states, we found no significant difference (difference in peak
167 values, paired t-test, $p = 0.5$). Furthermore, choice axes independently defined in low- and high-
168 attention states were highly correlated (Pearson's $r = 0.72 \pm 0.03$). Together, these results indicated
169 that the choice subspace defined by left and right trajectories remained the same across attention
170 states, but attention enabled difficulty-dependent modulations of the trajectories (Fig. 3j).

Distinct spatial and temporal characteristics of choice signals

171 Choice signals were broadly distributed across multiple areas, with distinct spatial and temporal
172 characteristics. We defined a spatial-distribution index (SDI) that captured whether several or only a few
173 areas contributed prominently to the d' discriminability and found that choice had the largest SDI values
174 (30 ± 4 %) compared to sensory, movement, and attentional signals (around 10 %) (Fig. 4a). Distinct
175 inter-area signatures of choice signals were also evident in the pairwise angular separation between
176 state axes (Fig. 4b). We found that, overall, angular distances were greater than 50° , with the choice axis
177 being near-orthogonal to the sensory, movement, and attention-related axis. In time, choice axes
178 computed separately before (-0.1 s) and after (0.3 s) movement onset were stable in the pre- and post-
179 movement periods and orthogonal to each other. Sensory and movement components had large angles
180 (around 70°), and the smallest angles (still over 45°) were observed between the movement and
181 attentional axes.

182 To examine area contributions to these differences, we performed a correlation analysis
183 between d' maps; for example, d' maps for stimulus and movement components (Fig. 2e, f) had overall
184 similar discriminability, but highlighted distinct area-specific contributions and, accordingly, the
185 correlation between the maps was small (Fig. 4c). We systematically analyzed all pairwise correlations
186 and used hierarchical clustering to identify components with stronger similarity in d' spatial distributions
187 (Fig. 4d). The stimulus axis was most dissimilar from others, followed by the cluster of choice axes.
188 Attention and movement components clustered together, consistent with their individual large pairwise
189 correlation values ($r > 0.5$, Fig. 4c).

190 To further examine the area-specific contributions to choice signals, we divided higher visual
191 areas into three main groups—ventral (L), dorsal (PM, AM), and parietal (A, RL, AL)³⁰—and separately
192 analyzed somatosensory (SSt, SSb) and retrosplenial (RS) regions. V1 contributed an overall uniform d'
193 value to all separations (Extended Data Figs. 2 and 6); hence, we did not include it in this analysis of
194 relative differences. We then computed d' values using only the locaNMF components that originated
195 from these grouped areas and did this for all variables: visual, movement, choice, and attention. This
196 resulted in a five-dimensional (5D: ventral, dorsal, parietal, somatosensory and retrosplenial) space,
197 where the coordinates of a variable reflected the contribution of a given region to the d' separability of
198 that variable. When examining discriminability power in 2-D projections of this 5-D space (Fig. 4e), we
199 found that regions contributing to choice were distinct from those of other components—including
200 movement—being most prominent in ventral stream regions, as reflected by the large d' values
201 observed in these areas (Extended Data Fig. 6). Ventral regions significantly contributed to visual
202 components, as expected, while dorsal and parietal regions contributed to movement variables—
203 especially wheel movements—in agreement with a previous report³⁵. Retrosplenial and somatosensory
204 areas contributed similarly to choice and movement, with d' values generally correlated across all
205 variables ($r = 0.8$; 95% confidence intervals (0.61, 0.97), for d' correlations between somatosensory and
206 retrosplenial areas across animals).

207 In summary, distributed choice signals were distinct from sensory, movement, and attentional
208 components, dominantly in ventral-stream visual areas and modulated by task difficulty and attention,
209 suggesting that they might reflect the decision-making computations associated with the discrimination
210 task.

RNN modeling of decision dynamics

211 To examine this possibility, we used RNNs as implementation-level, mechanistic models of the decision-
212 making process. Building on previous work showing that RNNs can capture decision-making
213 computations associated with 2AFC discrimination tasks^{23,24}, we examined the dynamics of RNNs trained

214 according to the invariance for absolute orientations built into our task—and learned by the animals.
215 Furthermore, we trained RNNs with the actual trial-to-trial choices of the animals, rather than using the
216 optimal task solution, and introduced variability in attention states (Fig. 5a). Using the animals' choices
217 rather than the task rule, created numerous “contradictory” examples, where the input evidence for a
218 left or right choice was non-deterministically associated with left or right output decisions, even in the
219 easiest trials (e.g., non-zero lapse rate). As a result, although RNNs were trained to produce L/R binary
220 choices, they learned analogue outputs that followed a psychometric probability function (Fig. 5a).
221 Furthermore, output amplitudes depended only on task difficulty, reflecting a learned invariance for
222 absolute orientations. Context-dependent attention modulations (introduced as an additional binary
223 input) modified output probabilities and created shallower or steeper psychometric curves in low or
224 high attention states respectively (Fig. 5a, Extended Data Fig. 4). Although the model was trained only
225 with a subset of 13 difficulties and 2 attention states, it was able to generalize to any difficulty level and
226 range of attention within the trained boundaries (Fig. 5b). We then analyzed the internal dynamics of
227 the network by computing choice and attention axes from RNNs unit responses, as we did for the neural
228 data with locaNMF components. In the RNNs also, the choice axis identified a decision variable that
229 represented L/R decisions as separate trajectories in a low-dimensional embedding space. Furthermore,
230 the separation between trajectories was modulated by task difficulty, with larger separations in easy
231 trials. This separation did not depend on absolute orientations, as expected from the RNN having
232 learned this invariance. The choice axis was stable across levels of difficulty (Fig. 5c). Attentional
233 modulations maintained an invariant representational geometry of the DV across the embedding space
234 (Fig. 5d-h). This was consistent with observations of the neural data, where choice and attention axes
235 were near-orthogonal with each other (Fig. 4b). In summary, the representational similarity between the
236 RNN and neural dynamics, together with the lack of neural information provided to the network,
237 indicated that the contextually-modulated choice signals observed in locaNMF components indeed
238 represented the decision-making computations underlying the orientation discrimination task.

Discussion

239 Using a tensor decomposition method that retained the spatial information in the responses, and
240 applied to mesoscale recordings in mouse dorsal-parietal cortices, we isolated choice signals that were
241 near-orthogonal to sensory-, movement- and attention-related variables. We showed that their
242 representational dynamics was consistent with the decision-making computations underlying the
243 behavioral task. We also showed that choice signals, although broadly distributed, were prominent in
244 ventral-stream visual areas and were modulated by task difficulty, with this modulation enabled
245 contextually by the attention state of the animal. Together, these results suggest a multiplexed

246 representation of variables in the posterior cortex, with a widespread distribution of decisional
247 information, possibly reflecting probabilistic inference computations; for instance, information about
248 the ongoing decision-making process could be used for perceptual inference with unreliable sensory
249 stimuli, and to influence sensory-to-decision signal transformations that inform future action plans.

Methodological relevance

250 We achieved these results by combining two powerful methods for the analysis of population
251 responses: locaNMF and activity-mode analysis. LocaNMF reduced the dimensionality of the neural data
252 while retaining spatial information, which would have been lost with traditional dimensionality
253 reduction methods (e.g., PCA). Furthermore, the state space representation allowed further reduction
254 of dimensionality while aligning the dynamics along task and decision-relevant dimensions. This latter
255 step took place within an interpretable linear framework, where the angle between the state axes and
256 d' values could be directly linked to the linear discriminability of the underlying variables. The imaging
257 methodology and task design used in this study facilitated the identification of distributed choice signals
258 encoded by sparse populations of cells⁴⁴ thanks to the local integration of these responses.
259 Furthermore, the complexity of the decision-making task might have influenced the wide spatial
260 distribution of the representations⁴⁵.

Feedback origin of choice signal

261 Choice signals emerged after stimulus onset, were broadly distributed in the posterior cortex, and could
262 be significantly detected as early in the visual hierarchy as in V1, suggesting feedback activations from
263 areas causally involved in the decision-making process. Other non-sensory signals identified in our
264 recordings, e.g. related to body and eye movements, could also result from feedback activations.
265 Indeed, feedback signals to the posterior cortex have been extensively documented in the literature, in
266 association with a great diversity of underlying variables and computations, including attentional
267 modulations⁴¹, movement-associated responses²⁸, sensory context⁴², and predictive coding⁴³.

Choice signals have distinctive spatial and temporal signatures

268 The properties of the choice signals met several criteria that are characteristic of a decision variable.
269 Their pre-movement components suggested that they did not simply reflect the execution of a motor
270 plan, nor an “unsigned” pre-motor, preparatory state⁴⁶. Choice signals did not simply reflect bottom-up,
271 stimulus-related information that correlated with the decision process because, given the task design,
272 the contra-lateral stimulus orientation was uninformative for L/R decisions²⁰, and furthermore, at the
273 mesoscale resolution used in this study, orientations were not decodable from the neural signal⁴⁷.

274 Choice signals could be separated from movements. The cortical localization of movement
275 components was prominent in dorsal-stream regions, consistent with previous reports^{28,35}. Choice
276 signals were localized in retrosplenial cortex, and in the visual cortex, mostly in ventral stream regions,
277 along the so-called “what” visual pathway⁴⁸. This was consistent with the task requirements: mice had to
278 evaluate the orientation “content” of both stimuli and make relative orientation comparisons. Absolute
279 orientations were informative, as were the locations of the stimuli, which were the same across trials;
280 thus, in contrast to “where” type of information, which is supposedly associated with dorsal stream
281 regions, solving the task relied on “what” information in the ventral stream areas.

282 We also controlled ventral-stream responses did not link to eye movements (Extended Data
283 Figure 7), which typically followed whole body movements³⁵. However, it is still possible that signals
284 detected in ventral areas were associated with motor-related components that also carried choice-
285 relevant information⁴⁹.

286 Attention-mediated modulations were orthogonal to the subspace defined by choice variables, with
287 the choice axis remaining significantly autocorrelated across time irrespective of attentional state. This
288 can be described as an isomorphic transformation in the embedding space of the decision variable (DV),
289 where the subspace defined by the L/R trajectories is *shifted*, without deforming the representational
290 geometry. The dependence of the decision variable on task difficulty was clearer in high-attention trials,
291 but not significant in low-attention states. This might reflect an actual dependence of the decision-
292 making process on attention, since in low-attention states mice might commit to a difficulty-
293 independent heuristic strategy.

294 The analysis of angles between state axes highlighted a large angular separation between variables,
295 with sensory and movement axes having the smallest separation. This latter observation agreed with
296 previous reports both at the local scale of small neuronal assemblies⁵⁰, and at the mesoscale³⁵,
297 indicating a covariability axis between these variables. Similarly, the smaller angles observed between
298 the movement axis and the attentional axis agreed with a recent report showing that attention
299 enhances distinctive spatial features in movement-related activations across these cortical regions³⁵.

RNN implementation and mechanistic insights

300 Recurrent state-space models, including RNNs, have been previously used in mechanistic investigations
301 of decision-making processes^{23,24}. Moreover, representational similarity analysis of the state-space of
302 RNNs and neural responses has been successfully used to infer underlying computations²³. Here, we
303 adopted a similar approach, but with three main distinguishing features. First, we trained the network
304 with the animals’ decisions, rather than the task rule. This constituted a significant departure from
305 previous research, which added noise to fully-deterministic RNNs to capture logistic behavioral tuning

306 functions^{24,51}. Instead, we trained the network with “contradictory” information, such as that involved in
307 the inconsistent trial-to-trial animals’ decisions, thus exposing the network to the biases and heuristics
308 of the animals. Training with the animal choices was akin to training with label noise, for which many
309 deep learning algorithms are robust⁵². The RNN outputs effectively implemented two dynamic
310 *accumulators* providing time-dependent scores for L/R choices, with the difference between the scores
311 being proportional to the psychometric function. This result was probably related to the mathematical
312 observation that if L/R choices were determined by two accumulators (for the left or right evidence,
313 respectively), the log-likelihood ratio of the conditional probabilities for a given choice, given the state of
314 the accumulators, can be shown to be proportional to the psychometric (logistic) function^{53,54}. The
315 second novelty was that we trained the RNN to learn an invariance regarding absolute orientations,
316 which were uninformative for the task choice. Finally, the third novelty concerned attentional
317 modulations. As observed in the neural data, the added attentional input to the RNN caused an
318 isomorphic shift of the decision-making manifold, which retained the geometry of the decision variable.
319 Geometry-preserving isomorphic shifts in low dimensional embedding spaces, might reflect a general
320 ‘decorrelation’ principle for variables that are concurrently represented across overlapping cortical
321 networks. These results confirmed that, mechanistically, the representational dynamic of choice signals
322 reflected the decision-making computations underlying the animals’ psychophysical behavior.

Limitations and open questions

323 Our results raise several questions to be addressed in future studies; for instance, it is unclear whether
324 the broad distribution of choice signals mirrored equally broad spiking activations. Regarding anatomical
325 considerations, feedback signals are known to preferentially target deep layers (five and six) and layer
326 one⁵⁵. Considering that our imaging microscope focused on superficial cortical layers and that GCaMP
327 was expressed across the cortex, it is possible that choice signals reflected long-range axon-terminal
328 activations and /or depolarizations in apical dendritic trees, rather than somatic firing. Concurrent
329 imaging and electrophysiological recordings across layers would clarify this point.

330 Our study relied on correlative measures, therefore loss- and gain-of-function perturbative
331 experiments will be necessary to establish causality. Of particular interest would be the inactivation of
332 lateral visual areas in view of the observed ventral-stream prominence. Furthermore, patterned
333 optogenetic methodologies with single-cell resolution might enable the stimulation of the individual
334 neurons that most significantly carry choice-relevant information in these regions.

335 In sum, broadly distributed feedback decision signals, having a representational dynamics
336 consistent with decision-making computations underlying the perceptual task, might represent an
337 activity—and computational—substrate capable of “molding” early sensory processing and sensory to

338 decision transformations depending on the underlying decision-making process for probabilistic-
339 inference computations in changeable agent-environment interactions⁵⁶.

Online Methods

340 Experimental procedures

341 Details of the experimental procedures (surgeries, behavioral training, recordings of body and eye
342 movements, imaging methods, and pre-processing of fluorescence data) have been described in
343 Abdolrahmani and collaborators³⁵. We summarize them here in brief.

344 Surgeries

345 All surgical and experimental procedures were approved by the Support Unit for Animal Resources
346 Development of RIKEN CBS. The transgenic mice used in this work were Thy1-GCaMP6f mice ($n = 7$). For
347 all reported results, the number of sessions per animal ranged from 9 to 60, with a minimum and
348 maximum number of trials per animal of 1,000 to 8,000. Animals were implanted with cranial posts for
349 head fixation and a round chamber (around 6mm diameter) for optical access to neural recordings.

350 Behavioral training

351 Animals were trained on a 2AFC orientation discrimination task. Two oriented Gabor patches were shown
352 on the left and right sides of a screen positioned in front of the animals at $\pm 35^\circ$ eccentricity relative to the
353 body's midline. Mice had to report which of the two stimuli matched a target orientation (vertical, $n = 5$;
354 horizontal, $n = 2$). The smallest orientation difference varied depending on the animals, from 3° to 30° .
355 The largest difference—the easiest discrimination—was $\pm 90^\circ$. Animals signaled their choice by rotating a
356 rubber wheel with their front paws, which shifted stimuli horizontally on the screen. For a response to be
357 correct, the target stimulus had to be shifted to the center of the screen, which led to the animal being
358 rewarded with 4 μL of water. Incorrect responses were discouraged with a prolonged (10 s) inter-trial
359 interval and a flickering checkerboard stimulus (2 Hz). If no response was made within 10 s (time-out
360 trials), neither reward nor discouragement was given. Animals were imaged after exceeding a
361 performance threshold of 75 % correct rate for 5–10 consecutive sessions. To work with a coherent
362 behavioral dataset, we excluded sessions with exceedingly large fractions for time-outs ($\geq 20\%$) or with
363 average performance below 60 %. Every trial consisted of an open-loop period (OL: 1.5 s) and a closed-
364 loop period (CL: 0–10 s), followed by an inter-trial interval (ITI: 3–5 s randomized). We recorded cortical
365 responses, wheel rotations, and eye/pupil videos from a pre-stimulus period (1 s duration) until the end
366 of the trial. Stimuli were presented in the OL period, during which wheel rotations did not produce any
367 stimulus movement.

368 Saccades, pupil area, and body movements

369 We monitored the contralateral eye using a CMOS camera. Automatic tracking of the pupil position was
370 done with custom software (Matlab, Mathworks®). We confirmed the accuracy of pupil tracking by
371 visually observing hundreds of trials. Saccade detection was achieved by applying an adaptive elliptic
372 thresholding algorithm to saccade velocities. We discarded saccades that lasted ≤ 60 ms and were
373 smaller than 1.5° . We extracted the time, magnitude, duration, velocity, start, and landing positions of

374 each saccade. We calculated the average pupil area for each imaging session by averaging area values
375 across all trials within the session. The pupil area in every trial was z-scored for each session.

376 Wheel detection

377 We recorded wheel rotations with a rotary encoder and flagged as potential wheel movements the time
378 points when the velocity had a zero-crossing (i.e., a sign change) and deviated from zero above a fixed
379 threshold (20°).

380 Imaging

381 Mice were placed under a microscope for wide-field imaging in tandem-lens epifluorescence
382 configuration. We imaged GCaMP6f fluorescent signals using a CMOS camera (pco.edge 5.5).

383 Pre-processing of fluorescence data

384 We motion corrected GCaMP data using a semi-automated control-point selection method (MATLAB
385 *cpselect*). To compute relative fluorescence responses, we calculated a grand-average scalar $F_0^{i,j} = \langle$
386 $I_{x,y,t}^{i,j} \rangle_{x,y,t}$, with $I_{x,y,t}^{i,j}$ representing the XYT image tensor in trial i , session j . We then used this scalar to
387 normalize the raw data tensor $F_{x,y,t}^{i,j} = (I_{x,y,t}^{i,j} - F_0^{i,j}) / F_0^{i,j}$. The data for each trial were then band-pass
388 filtered (0.1 to 12 Hz). Each tensor was compressed with spatial binning (130×130 μm^2 with 50% overlap).
389 Trial data was further downsampled to 30 fps and low-pass filtered with a cutoff at 8 Hz.

390 Retinotopy

391 We used a standard frequency-based method (Kalatsky and Stryker, Neuron 2003) with slowly moving
392 horizontal and vertical flickering bars. Visual area segmentation was performed based on azimuth and
393 elevation gradient inversions. To center and orient maps across animals, we used the centroid of area V1
394 and the iso-azimuth line passing through it.

395 Alignment to the Allen Mouse Brain Common Coordinate Framework

396 Imaging data from each animal was aligned to the Allen Mouse Brain Common Coordinate Framework
397 (CCF) following the approach described by Waters (Waters et al., Plos One, 2019). In brief, we extracted
398 the centroids of areas V1, RL and PM, using them to create a triangle that we aligned to the one from
399 the Allen CCF by first making the V1 vertices coincide. We then rotated and scaled the triangle to
400 minimize the distance between the other vertices while maintaining the original angles.

401 Data processing

402 LocaNMF

403 LocaNMF analysis was conducted following the methods described by Saxena (Saxena et al., PLOS Comp.
404 Biol. 2020). Briefly, imaging data across all trials and sessions was first concatenated and its
405 dimensionality reduced using singular-value decomposition (SVD) up to 99 % of the original variance.
406 LocaNMF was initialized using 10 regions based on the Allen CCF and corresponding to V1 (VISp), PM

407 (VISpm), AM (VISam), A (VISa), SSt (SSp-tr), RL (VISrl), SSb (SSp-bfd), AL (VISal), L (VISl and VISli), and RS
 408 (RSPagl and RSPd) (Extended Data Figure 1). A masking region was created for each area by setting a
 409 distance $D = 1$ within the region boundaries and an exponential decrease (to zero) for pixels outside the
 410 boundary. The localization penalty for each pixel was $1-D$ (Extended Data Figure 1). LocaNMF rank line
 411 search was run for these 10 regions with a localization threshold of 75 % and total explained variance of
 412 99 %, resulting on average in approximately 200 components per animal. After decomposition, temporal
 413 components were separated back into the original trial structure. More formally, LocaNMF produced a
 414 decomposition tensor $F_{x,y,t}^i \sim \sum_k A_{x,y,k} C_{k,t}^i$ for trial i , where $A_{x,y,k}$ is the spatial part of component k ,
 415 and $C_{k,t}^i$ is its temporal part. The spatial parts of the components were significantly localized and could
 416 be mapped onto the original seeding area. The temporal component captured the unique trial-to-trial
 417 variability, and all subsequent analyses in the time domain were conducted using only the temporal $C_{k,t}^i$
 418 of locaNMF components. Total explained variance (EV) of the decomposition, was computed by
 419 projecting one component at a time across the whole time series and checking the relative explained
 420 variance across pixels with the original recording.

421 Global State Vector definition

422 We defined a state vector as a one-dimensional projection of locaNMF temporal components $\mathbf{C}(t)$ that
 423 maximized the weighted distance between the trajectories of two trial groups **A** and **B** (bold letters
 424 indicate vectors). For each trial group, we defined average trajectories $\langle \mathbf{A}(t) \rangle$ and $\langle \mathbf{B}(t) \rangle$ and defined
 425 $\mathbf{S}(t) = \left\| \frac{\langle \mathbf{A}(t) \rangle - \langle \mathbf{B}(t) \rangle}{\sigma_{AB}(t)} \right\|$, where $\sigma_{AB}(t) = \sqrt{\frac{1}{2}(\sigma_{A(t)}^2 + \sigma_{B(t)}^2)}$ is the pooled standard deviation between
 426 the two groups. State vector projections for the i -th trial were then obtained by the dot product $P^i(t) =$
 427 $\mathbf{S}(t) \cdot \mathbf{C}^i(t)$, where $\mathbf{C}^i(t)$ are the temporal locaNMF components of trial i . Discriminability between the
 428 original A and B groups was then computed as $d' = \frac{\langle P_A^i(t) \rangle - \langle P_B^i(t) \rangle}{\sigma_{P_A P_B}(t)}$ (i.e., the difference between the
 429 averaged projections of groups A and B, divided by their pooled standard deviation). To validate state
 430 vectors, projections, and discriminability, we performed five-fold cross validation, i.e., state vectors
 431 were defined using only 20% of the trials of each group and projections and d' were computed on the
 432 remaining trials.

433 State-vector stability

434 To assess the stability of state vectors, we computed instantaneous state vectors $\mathbf{S}(t)$ using a
 435 “backward” three-frame averaging window (around 100 ms) and then computed its temporal
 436 autocorrelation $C(\mathbf{S}(t), \mathbf{S}(t'))$. For sensory, movement, and sustained attention state vectors, we chose
 437 the time-independent state vector $\mathbf{S} \equiv \mathbf{S}(t^*)$, where t^* was chosen from the largest stability cluster
 438 (represented by a gray bar in the respective figures). For the state vector of choice, we used the original
 439 $\mathbf{S}(t)$ to monitor when choice information first appeared and whether its signature was unique.

440 Area-specific state vectors

441 We defined state vectors for each of the 10 areas by only using the subset of locaNMF components $C_{k,t}^i$
442 that originated from that area. This was akin to first projecting onto the subspace defined by the
443 components of a particular area, and then obtaining the associated state vector.

444 Task-related state vectors

445 Stimulus: For stimulus state-vectors, we used for the first group (**A**) all the trials in the time interval (-0.5
446 to +0.5 s) centered on the stimulus onset. For group **B**, since the stimulus was present in all trials, we
447 used the same trials in the (-1 to 0 s) interval before stimulus presentation.

448 Contralateral stimulus (Extended Data Fig. 3): We used trials with the left stimulus horizontal as group **A**
449 and the trials with the left stimulus vertical as group **B**.

450 Wheel movement: Group **A** consisted of trials for which the first movement after stimulus presentation
451 occurred at least 0.5 s after stimulus onset and without any saccades detected in the previous 0.5 s.
452 These trials were aligned to the detected movement onset. Group **B** consisted of trials with no
453 movement detected during the first 5 s after stimulus onset. These trials were aligned by taking a
454 random frame within the same time interval.

455 Saccades defined as for wheel movements.

456 Sustained attention: Sustained attention was measured by changes in pupil area during the trial. We
457 computed the pupil change measure, 'pA', as the difference between the maximum pupil area after
458 stimulus onset and the average area 1 s before stimulus onset. We labeled as "high-attention" trials
459 (group **A**) those in the top 33rd percentile of the pA distribution and as "low-attention" trials (group **B**)
460 those in the bottom 33rd percentile.

461 Choice: L/R choices in each trial were measured from the direction of the first movement after stimulus
462 onset. The state vector for group **A** was computed from right-choice trials and for group **B** using left-
463 choice trials. As for the detection of wheel movements, we restricted the analysis to trials in which the
464 first movement occurred at least 0.5 s after stimulus onset and with no saccades 0.5 s before the
465 detected movement. Trials were aligned to the time of movement detection.

466 Piecewise linear fitting of d' curves

467 To fit the time-evolving d' curves to periods before and after movement onset, we performed two-slope
468 piecewise linear fitting using the Shape Language Modeling toolbox (MATLAB Central File Exchange,
469 John D'Errico, 2021; SLM—shape language modeling;
470 <https://www.mathworks.com/matlabcentral/fileexchange/24443-slm-shape-language-modeling>). This
471 method performs two linear fits in a fixed interval with a single knot between them. We chose the
472 interval -1 s before movement onset up to the 95th percentile of the peak post-movement response
473 amplitude (typically occurring around 0.3 s after movement onset). The position of the knot determined
474 the slope change time.

475 Spatial-Distribution Index (SDI)

476 The SDI for a given state vector was computed as $SDI (\%) = \left(\frac{d'_{global}}{\max(d'_i)} - 1 \right) \cdot 100$ where d'_i refers to the
477 area- specific d' scores.

478 RNN Model

479 The RNN consisted of a single RNN module with $N = 128$ neurons (ReLU activations), receiving 3 inputs
480 (left stimulus, right stimulus, and attention level) and producing a binary response as an output for left
481 or right choices (softmax activation).

482 Inputs: The input space consisted of a sequence of 25 frames. Stimulus orientations were mapped to the
483 range of -1 to +1 (corresponding to -90 to +90°) and were presented after the first 10 frames. The
484 difficulty of a trial was encoded by the absolute difference between the two stimulus signals. Attention
485 was modeled as a constant binary signal (0 or 1), already present at the beginning of the trial. A small
486 noise (normally distributed with amplitude 0.01) was added to the input signals to improve the
487 robustness of the optimization, but it was irrelevant for the psychometric fitting.

488 Training: For training the network, we generated simulated animal responses by computing L/R choices,
489 following a psychometric curve of the form $P_{left}(\theta) = \frac{1}{1+e^{-\alpha\theta}} (1 - \lambda) + \frac{\lambda}{2}$, where θ is the difference
490 between the two inputs, λ is the lapse rate, and α controls the slope. We used a constant $\lambda = 0.1$ and
491 $\alpha = 3/90$ for low attention and $\alpha = 10/90$ for high attention; that is, attention decreased the amount
492 of label noise during training. To train the network, we used 6,400 trials per difficulty level and chose 13
493 difficulty levels with angle differences uniformly distributed from -90 to +90 degrees. We trained the
494 network using a batch normalization layer and a custom loss function consisting of the categorical cross
495 entropy at the time of stimulus presentation and in the last frame. We included the stimulus
496 presentation time in the loss function to prevent the output drifting before stimulus presentation,
497 following a procedure used by Mante (Mante et al., Nature 2013). Accuracy during training was
498 computed using the categorical accuracy at the end of the trial. The network was implemented with
499 TensorFlow 2.0 and trained using the Adam optimizer for 25 epochs with a batch size of 640. Note that
500 training the network with the animal choices made the network robust to overfitting. We trained 10
501 different networks by generating new sets of inputs and randomly initializing the network weights.

502 Analysis: We analyzed the output of the RNN in the same way as for the neural data, but we used the
503 time series of the $N = 128$ neurons instead of the locaNMF components to define choice and attention
504 state vectors.

References

- 505 1. Macke, J. H. & Nienborg, H. Choice (-history) correlations in sensory cortex: cause or
506 consequence? *Curr. Opin. in Neurobiol.* vol. 58 148–154 (2019).
- 507 2. Crapse, T. B. & Basso, M. A. Insights into decision making using choice probability. *J.*
508 *Neurophysiol.* **114**, 3039–3049 (2015).
- 509 3. Britten, K. H., Newsome, W. T., Shadlen, M. N., Celebrini, S. & Movshon, J. A. A relationship
510 between behavioral choice and the visual responses of neurons in macaque MT. *Vis Neurosci* **13**,
511 87–100 (1996).
- 512 4. Kiani, R., Cueva, C. J., Reppas, J. B. & Newsome, W. T. Dynamics of neural population responses in
513 prefrontal cortex indicate changes of mind on single trials. *Curr Biol* **24**, 1542–1547 (2014).
- 514 5. Peixoto, D. *et al.* Decoding and perturbing decision states in real time. *Nature* 1–6 (2021).
- 515 6. Nienborg, H. & Cumming, B. G. Macaque V2 neurons, but not V1 neurons, show choice-related
516 activity. *Journal of Neuroscience* **26**, 9567–9578 (2006).
- 517 7. Grunewald, A., Bradley, D. C. & Andersen, R. A. Neural Correlates of Structure-from-Motion
518 Perception in Macaque V1 and MT. *J of Neurosci.* **22**, 6195–6207 (2002).
- 519 8. Steinmetz, N. A., Zatka-Haas, P., Carandini, M. & Harris, K. D. Distributed coding of choice, action
520 and engagement across the mouse brain. *Nature* **576**, 266–273 (2019).
- 521 9. Pho, G. N., Goard, M. J., Woodson, J., Crawford, B. & Sur, M. Task-dependent representations of
522 stimulus and choice in mouse parietal cortex. *Nat. Comms.* **9**, 2596 (2018).
- 523 10. Najafi, F. *et al.* Excitatory and inhibitory subnetworks are equally selective during decision-
524 making and emerge simultaneously during learning. *Neuron* **105**, 165-179.e8 (2020).
- 525 11. Uka, T. & DeAngelis, G. C. Contribution of area MT to stereoscopic depth perception: Choice-
526 related response modulations reflect task strategy. *Neuron* **42**, 297–310 (2004).
- 527 12. Shadlen, M. N., Britten, K. H., Newsome, W. T. & Movshon, J. A. A computational analysis of the
528 relationship between neuronal and behavioral responses to visual motion. *J Neurosci* **16**, 1486–
529 1510 (1996).
- 530 13. Haefner, R. M., Gerwinn, S., Macke, J. H. & Bethge, M. Inferring decoding strategies from choice
531 probabilities in the presence of correlated variability. *Nat. Neurosci.* **16**, 235–242 (2013).
- 532 14. Uka, T., Tanabe, S., Watanabe, M. & Fujita, I. Neural correlates of fine depth discrimination in
533 monkey inferior temporal cortex. *J. of Neurosci.* **25**, 10796–10802 (2005).
- 534 15. Jasper, A. I., Tanabe, S. & Kohn, A. Predicting perceptual decisions using visual cortical
535 population responses and choice history. *J. Neurosci.* **39**, 6714–6727 (2019).
- 536 16. Goris, R. L. T., Ziemba, C. M., Stine, G. M., Simoncelli, E. P. & Movshon, J. A. Dissociation of choice
537 formation and choice-correlated activity in macaque visual cortex. *J. Neurosci.* (2017).
- 538 17. McCormick, D. A., McGinley, M. J. & Salkoff, D. B. Brain state dependent activity in the cortex
539 and thalamus. *Curr. Opin. Neurobiol.* **31**, 133–140 (2015).

- 540 18. Miller, E. K. & Buschman, T. J. Cortical circuits for the control of attention. *Current Opinion in*
541 *Neurobiology* vol. 23 216–222 (2013).
- 542 19. Lange, R. D. & Haefner, R. M. Characterizing and interpreting the influence of internal variables
543 on sensory activity. *Curr. Opin. Neurobiol.* **46**, 84–89 (2017).
- 544 20. Lyamzin, D. R., Aoki, R., Abdolrahmani, M. & Benucci, A. Mice can learn a stimulus-invariant
545 orientation discrimination task. *bioRxiv* 2020.12.20.423700 (2020).
546 <https://www.biorxiv.org/content/10.1101/2020.12.20.423700v1>
- 547 21. Saxena, S. *et al.* Localized semi-nonnegative matrix factorization (LocaNMF) of widefield calcium
548 imaging data. *PLoS Comp. Biol.* **16**, e1007791 (2020).
- 549 22. Li, N., Daie, K., Svoboda, K. & Druckmann, S. Robust neuronal dynamics in premotor cortex
550 during motor planning. *Nature* **532**, 459–464 (2016).
- 551 23. Mante, V., Sussillo, D., Shenoy, K. v & Newsome, W. T. Context-dependent computation by
552 recurrent dynamics in prefrontal cortex. *Nature* **503**, 78–84 (2013).
- 553 24. Yang, G. R., Joglekar, M. R., Song, H. F., Newsome, W. T. & Wang, X. J. Task representations in
554 neural networks trained to perform many cognitive tasks. *Nat Neurosci* **22**, 297–306 (2019).
- 555 25. Wang, X. J. Decision making in recurrent neuronal circuits. *Neuron* **60**, 215–234 (2008).
- 556 26. Aoki, R., Tsubota, T., Goya, Y. & Benucci, A. An automated platform for high-throughput mouse
557 behavior and physiology with voluntary head-fixation. *Nature Comms.* **8**, (2017).
- 558 27. Burgess, C. P. *et al.* High-yield methods for accurate two-alternative visual psychophysics in
559 head-fixed mice. *Cell Rep.* **20**, 2513–2524 (2017).
- 560 28. Parker, P. R. L., Brown, M. A., Smear, M. C. & Niell, C. M. Movement-related signals in sensory
561 areas: Roles in natural behavior. *Trends Neurosci.* **43**, 581–595 (2020).
- 562 29. Wang, Q. *et al.* The allen mouse brain common coordinate framework: A 3D reference atlas. *Cell*
563 **181**, 936-953.e20 (2020).
- 564 30. Lyamzin, D. & Benucci, A. The mouse posterior parietal cortex: Anatomy and functions. *Neurosci.*
565 *Res.* **140**, 14–22 (2019).
- 566 31. Musall, S., Kaufman, M. T., Juavinett, A. L., Gluf, S. & Churchland, A. K. Single-trial neural
567 dynamics are dominated by richly varied movements. *Nat. Neurosci.* **22**, 1677–1686 (2019).
- 568 32. Averbeck, B. B. & Lee, D. Effects of noise correlations on information encoding and decoding. *J.*
569 *Neurophysiol.* **95**, 3633–3644 (2006).
- 570 33. Seung, H. S. & Sompolinsky, H. Simple models for reading neuronal population codes. *Proc. Natl.*
571 *Acad. Sci. USA* **90**, 10749–10753 (1993).
- 572 34. Ohki, K. *et al.* Highly ordered arrangement of single neurons in orientation pinwheels. *Nature*
573 **442**, 925–928 (2006).
- 574 35. Abdolrahmani, M., Lyamzin, D. R., Aoki, R. & Benucci, A. Attention decorrelates sensory and
575 motor signals in the mouse visual cortex. *bioRxiv* (2020).
576 <https://www.biorxiv.org/content/10.1101/615229v2>

- 577 36. Sommer, M. A. & Wurtz, R. H. Brain circuits for the internal monitoring of movements. *Annu.*
578 *Rev. Neurosci.* **31**, 317–338 (2008).
- 579 37. Esterman, M. & Rothlein, D. Models of sustained attention. *Curr. Opin. Psych.* vol. 29 174–180
580 (2019).
- 581 38. Sarter, M., Givens, B. & Bruno, J. P. The cognitive neuroscience of sustained attention: where
582 top-down meets bottom-up. *Brain Res. Rev.* **35**, 146–160 (2001).
- 583 39. Unsworth, N., Robison, M. K. & Miller, A. L. Pupillary correlates of fluctuations in sustained
584 attention. *J. Cogn. Neurosci.* **30**, 1241–1253 (2018).
- 585 40. Kiani, R. & Shadlen, M. N. Representation of confidence associated with a decision by neurons in
586 the parietal cortex. *Science* **324**, 759–764 (2009).
- 587 41. McAdams, C. J. & Reid, R. C. Attention modulates the responses of simple cells in monkey
588 primary visual cortex. *J. Neurosci.* **25**, 11023–11033 (2005).
- 589 42. Angelucci, A. *et al.* Circuits and mechanisms for surround modulation in visual cortex. *Annu. Rev.*
590 *Neurosci.* (2017).
- 591 43. Keller, G. B. & Mrsic-Flogel, T. D. Predictive processing: A canonical Cortical computation. *Neuron*
592 vol. 100 424–435 (2018).
- 593 44. Parker, A. J. & Newsome, W. T. Sense and the single neuron: probing the physiology of
594 perception. *Annu. Rev. Neurosci.* **21**, 227–277 (1998).
- 595 45. Pinto, L. *et al.* Task-dependent changes in the large-scale dynamics and necessity of cortical
596 regions. *Neuron* **104**, 810–824 (2019).
- 597 46. Elsayed, G. F., Lara, A. H., Kaufman, M. T., Churchland, M. M. & Cunningham, J. P. Reorganization
598 between preparatory and movement population responses in motor cortex. *Nat. Comms.* **7**,
599 13239 (2016).
- 600 47. Ohki, K., Chung, S., Ch'ng, Y. H., Kara, P. & Reid, R. C. Functional imaging with cellular resolution
601 reveals precise micro-architecture in visual cortex. *Nature* (2005).
- 602 48. Ungerleider, L. M. & Mishkin, M. Two cortical visual systems. in *Analysis of Visual Behavior* (eds.
603 Ingle, D. J., Goodale, M. A. & Mansfield, R. J. W.) (MIT Press, 1982).
- 604 49. Siegel, M., Buschman, T. J. & Miller, E. K. Cortical information flow during flexible sensorimotor
605 decisions. *Science* **348**, 1352–1355 (2015).
- 606 50. Stringer, C. *et al.* Spontaneous behaviors drive multidimensional, brainwide activity. *Science* **364**,
607 255 (2019).
- 608 51. Song, H. F., Yang, G. R. & Wang, X.-J. Training excitatory-inhibitory recurrent neural networks for
609 cognitive tasks: A simple and flexible framework. *PLoS Comput. Biol.* **12**, e1004792 (2016).
- 610 52. Rolnick, D., Veit, A., Belongie, S. & Shavit, N. Deep learning is robust to massive label noise. *arXiv*
611 **1705.10694**, (2017).
- 612 53. Gold, J. I. & Shadlen, M. N. Neural computations that underlie decisions about sensory stimuli.
613 *Trends. Cogn. Sci.* **5**, 10–16 (2001).

- 614 54. Bogacz, R. Optimal decision-making theories: linking neurobiology with behaviour. *Trends Cogn.*
615 *Sci.* **11**, 118–125 (2007).
- 616 55. Berezovskii, V. K., Nassi, J. J. & Born, R. T. Segregation of feedforward and feedback projections
617 in mouse visual cortex. *J. Comp. Neurology* **519**, 3672–3683 (2011).
- 618 56. Zagha, E. Shaping the cortical landscape: Functions and mechanisms of top-down cortical
619 feedback pathways. *Front. Sys. Neurosci.* **14**, 33 (2020).

Acknowledgments

620 We thank Rie Nishiyama, Yuka Iwamoto, and Yuki Goya for providing technical support for multiple
621 aspects of the experiments. We also thank O'Hara & Co., Ltd. for their support with the equipment. This
622 work was funded by RIKEN BSI and RIKEN CBS institutional funding; HFSP postdoctoral fellowship
623 LT000582/2019 awarded to J. O.; JSPS grants 26290011, 17H06037, 372 C0219129 awarded to A. B.; and
624 a Fujitsu collaborative grant.

Authors contributions

625 B. and J. O. conceived the project and wrote the manuscript; M. A., R. A., and D. L. collected the data; M.
626 A. and J. O. pre-processed the data and J. O. analyzed the data.

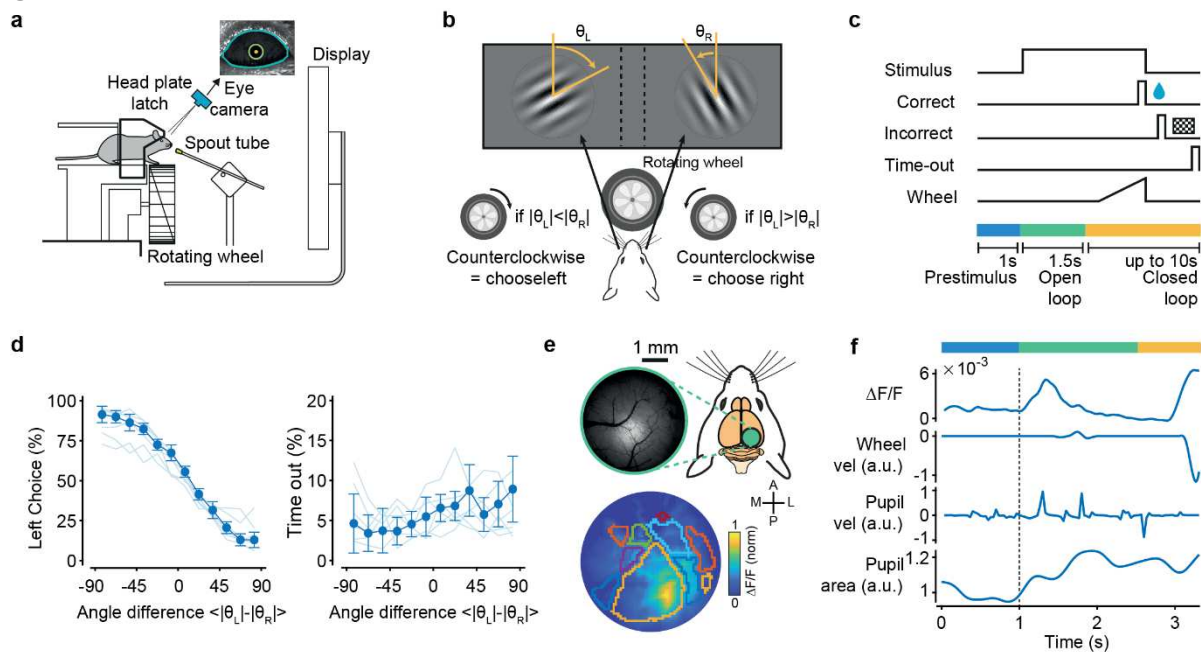
Data and code availability

627 Code for the analyses and source data for the figures will be made available upon acceptance of the
628 manuscript at <https://github.com/benuccilabnbc/dm>. All other relevant data will be made available by
629 the corresponding author upon reasonable request.

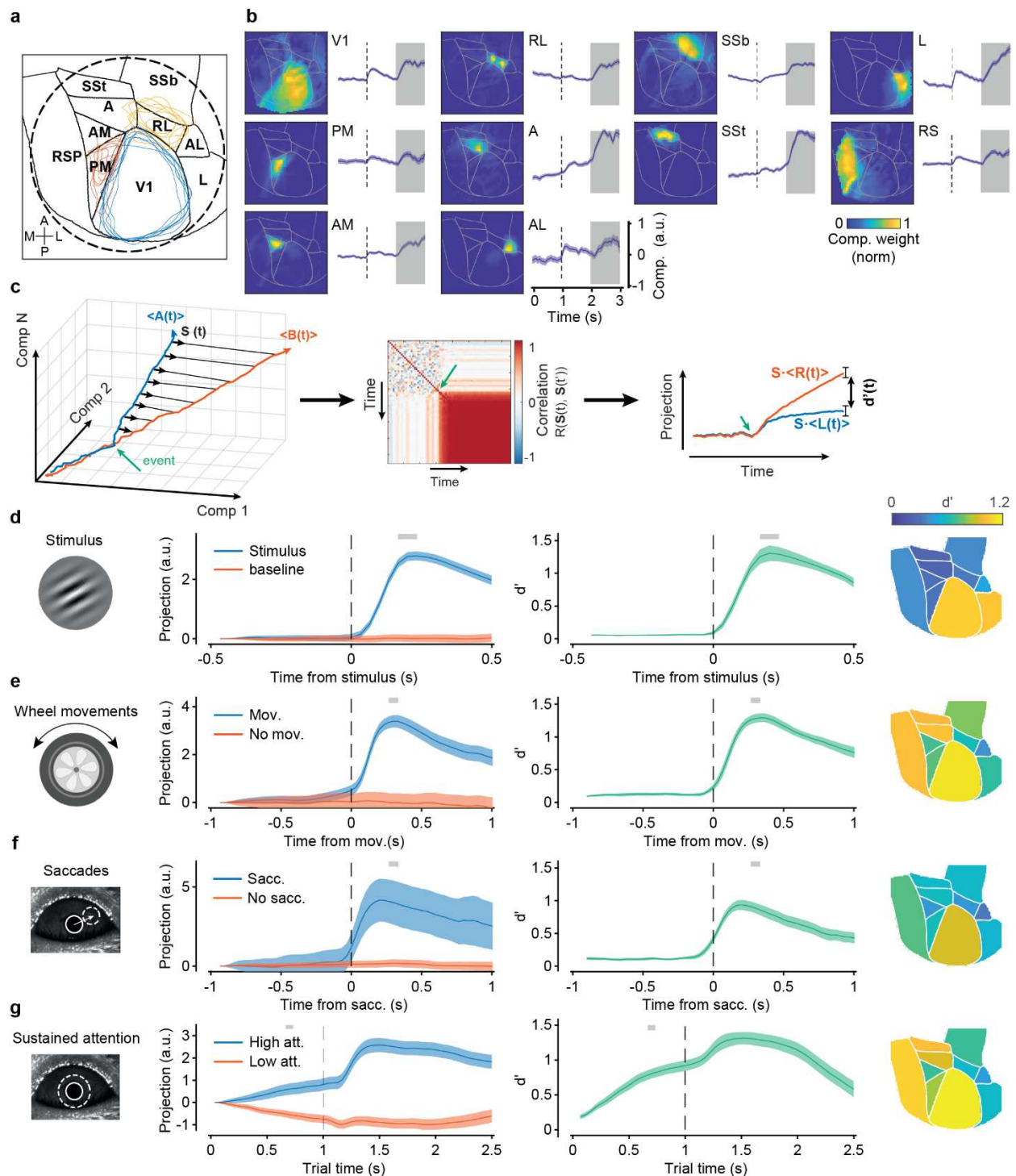
Competing Interests

630 The authors declare no competing interests.

Figures

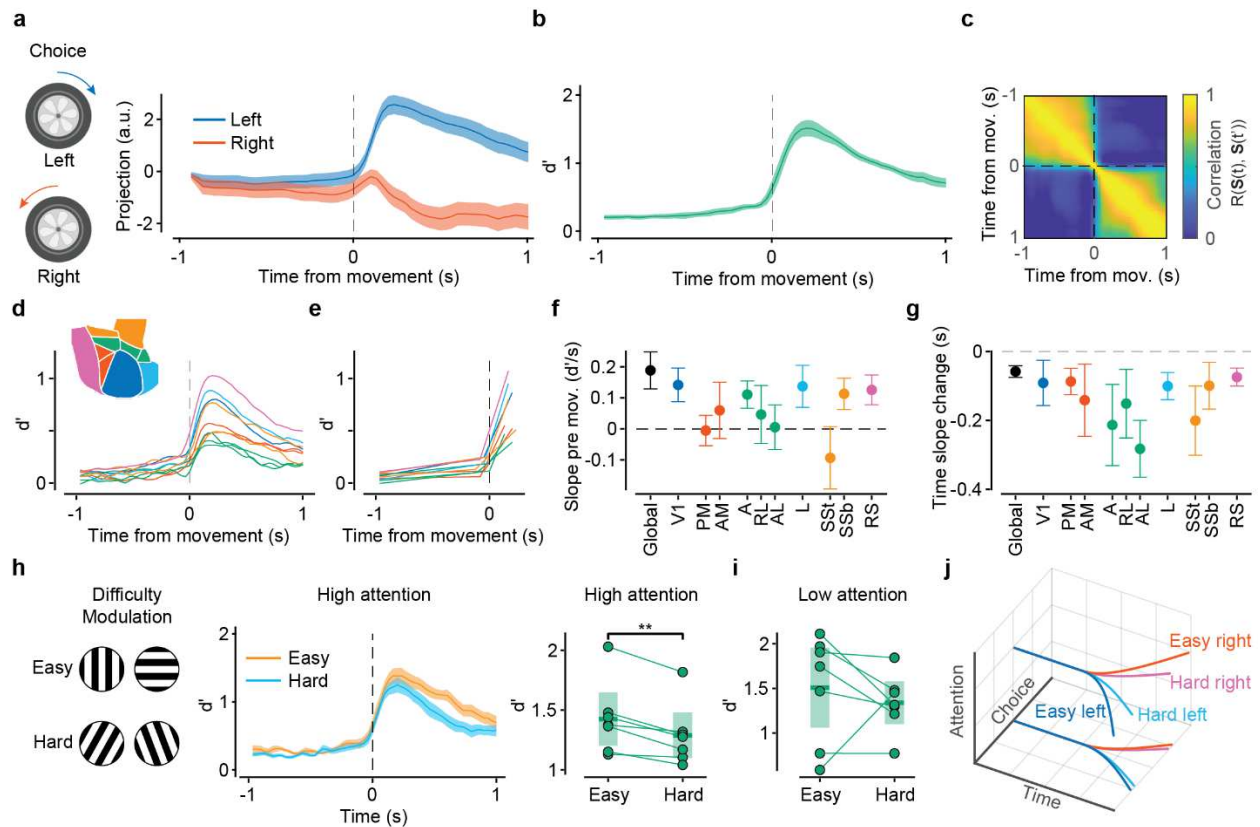


631 **Figure 1 | Imaging dorsal-parietal areas during an orientation discrimination task.** **a**, Mice were trained
 632 on a 2AFC orientation discrimination task using an automated setup featuring voluntary head fixation.
 633 They signaled a L/R choice by rotating a toy wheel with their front paws. **b**, Mice rotated the wheel to
 634 position the most vertical of two oriented gratings in the center of the screen. **c**, Trial structure: After a 1
 635 s pre-stimulus period, the stimulus was presented, followed by a 1.5 s OL interval in which wheel
 636 movements were decoupled from stimulus movements. Thereafter, in the CL period, wheel rotations
 637 resulted in L/R horizontal shifts of the stimuli. Correct choices were rewarded with water; incorrect
 638 choices were followed by a checkerboard pattern presentation. Ten seconds of no movement in the CL
 639 period triggered a time-out period. **d**, Left: mice's performance in the task (fraction of left choices) as a
 640 function of angle difference from the target orientation (nominal value of zero). Thick line = mean (\pm
 641 s.e.) across animals; thin lines = individual animals. Right: fraction of timeout trials as a function of
 642 difficulty. Timeout trials did not depend on task difficulty. **e**, Widefield calcium imaging of the posterior
 643 cortices of Thy1-GCaMP6f mice, with retinotopic mapping of 10–12 visual areas (colored contours). **f**,
 644 Simultaneously recorded fluorescence signals (dF/F), wheel and eye velocities, and pupil areas. In this
 645 example, choice was signaled at $t = 3.1$ s (by a sharp increase in wheel velocity).



646 **Figure 2 | LocaNMF decomposition identifies sensory, behavioral, and attention-related variables.** **a,**
647 Characteristic imaging window (dashed circle) superimposed on 10 cortical areas from the Allen Brain
648 Atlas reference framework. Blue, red, and yellow contours are the reference-aligned area boundaries for
649 V1, PM and RL for each animal. **b,** Spatial weights and trial-averaged time-series of the largest locaNMF
650 components for each of the 10 seeding regions (Extended Data Fig. 1) for a representative animal.
651 Selected trials for the trial-average all presented wheel movements within the 1 s shaded region. **c,**
652 Schematic for the definition of state vectors. The direction of the state vector becomes stable after an

653 event indicated by the green arrow. Vector stability is measured as the temporal autocorrelation $r(\mathbf{S}(t),$
654 $\mathbf{S}(t'))$, (right panel). Projections (cross-validated) of the two variables $\mathbf{A}(t)$ and $\mathbf{B}(t)$ onto \mathbf{S} separately over
655 time, as quantified by a d' discriminability measure. **d**, Stimulus-related state vector. Left: projections of
656 trials with and without a stimulus response onto the stimulus state vector for a given animal. Lines and
657 shaded regions indicate projection averages across trials and s.e. Middle: Discriminability d' over time,
658 averaged across all animals. Gray bars on top, epoch used for the time-average of the state vector.
659 Right: area-specific peak d' scores obtained by defining the state vector using only the components
660 originating from that area. **e**, As in **d**, but aligned to movement-detection time, i.e., separability between
661 trials with and without a detected wheel movement. **f**, As in **e**, but for saccadic eye movements. **g**, As in
662 **f**, but for sustained attention. High- and low-attention trials were defined based on pupil area changes,
663 using the highest or lowest 33rd percentile of the area-change distribution.



664

665

666

667

668

669

670

671

672

673

674

675

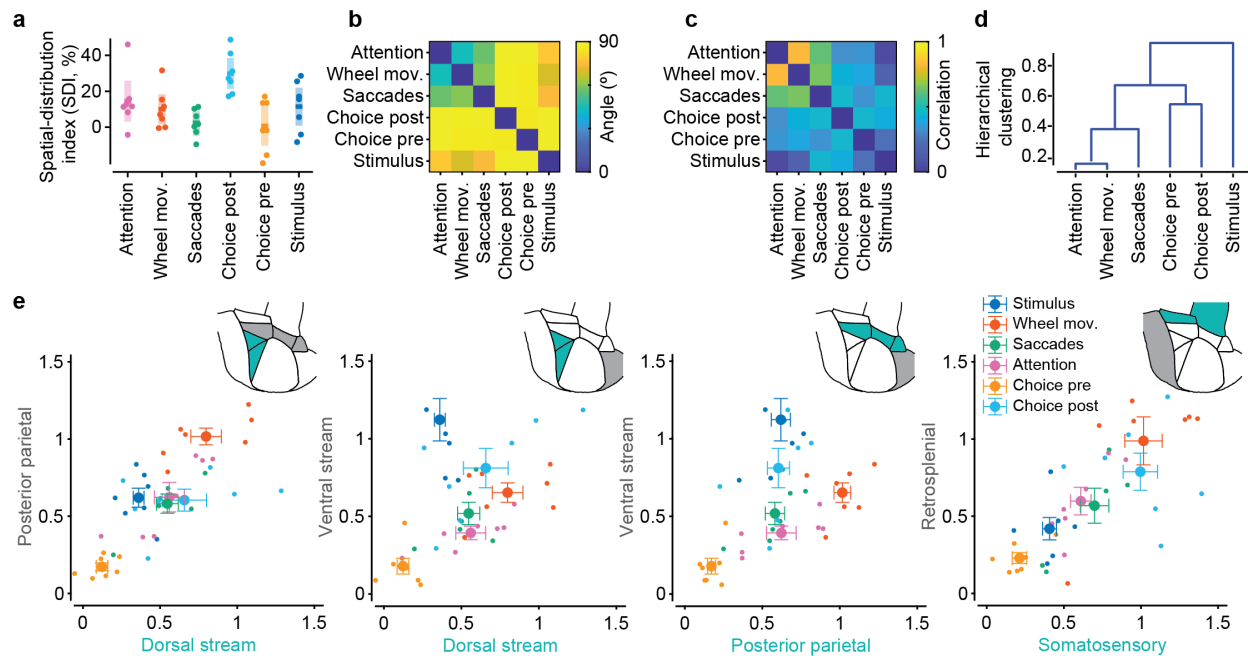
676

677

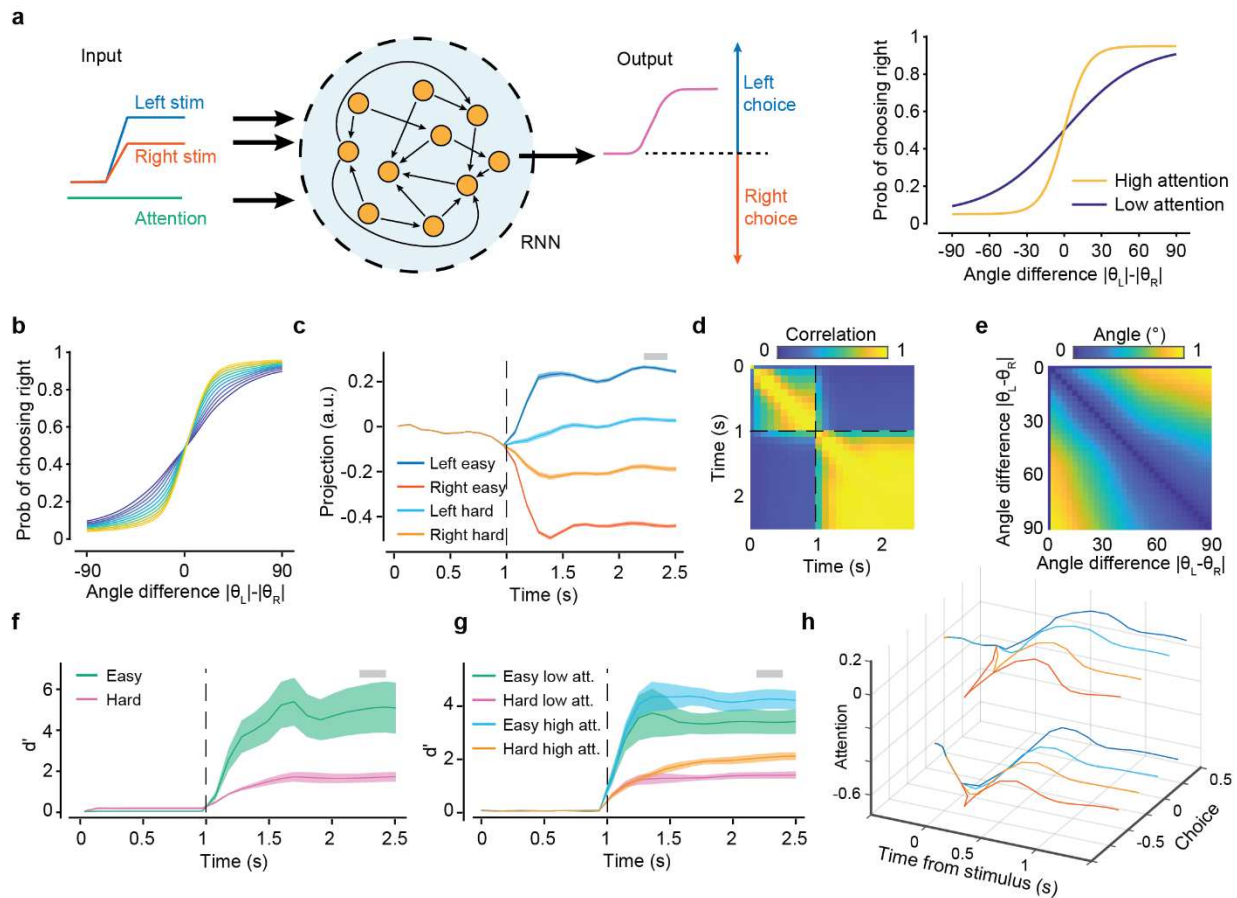
678

679

Figure 3 | Choice signals have pre-motor component and are modulated by task difficulty and attentions. **a**, Projections on the state vector for choice signals for a characteristic animal (line for trial average and shaded area for s.e.). Wheel movements signaling either a left or a right choice were aligned to the wheel movement onset. **b**, Evolution of d' discriminability relative to movement time averaged across animals. Early and late choice periods were defined relative to movement onset. **c**, Temporal stability of the state vector for choice. There is a clear change in the contribution of the choice state vector near the time of movement onset. Same animal as in **a**. **d**, Temporal evolution of area-specific d' curves (inset: area color code). **e**, Piecewise linear fits of the curves in **d** in pre- and post-movement periods. **f**, Pre-movement slopes fitted in **e** for different areas; error bars, 95% confidence intervals (CI) across animals. **g**, Times of slope change for different areas from the fits in **e**. Data and colors as in **f**. **h**, Left: evolution of choice discriminability, d' , in high attention states for easy and hard trials (angle difference $>$ or $<$ 45°). Right: Paired comparisons of peak d' values for each animal ($p = 0.003$). **i**, As in **h**, but for low-attention states. Paired differences were not significant ($p = 0.50$). **j**, Schematic representation of the temporal evolution of left and right trajectories with difficulty and attention.

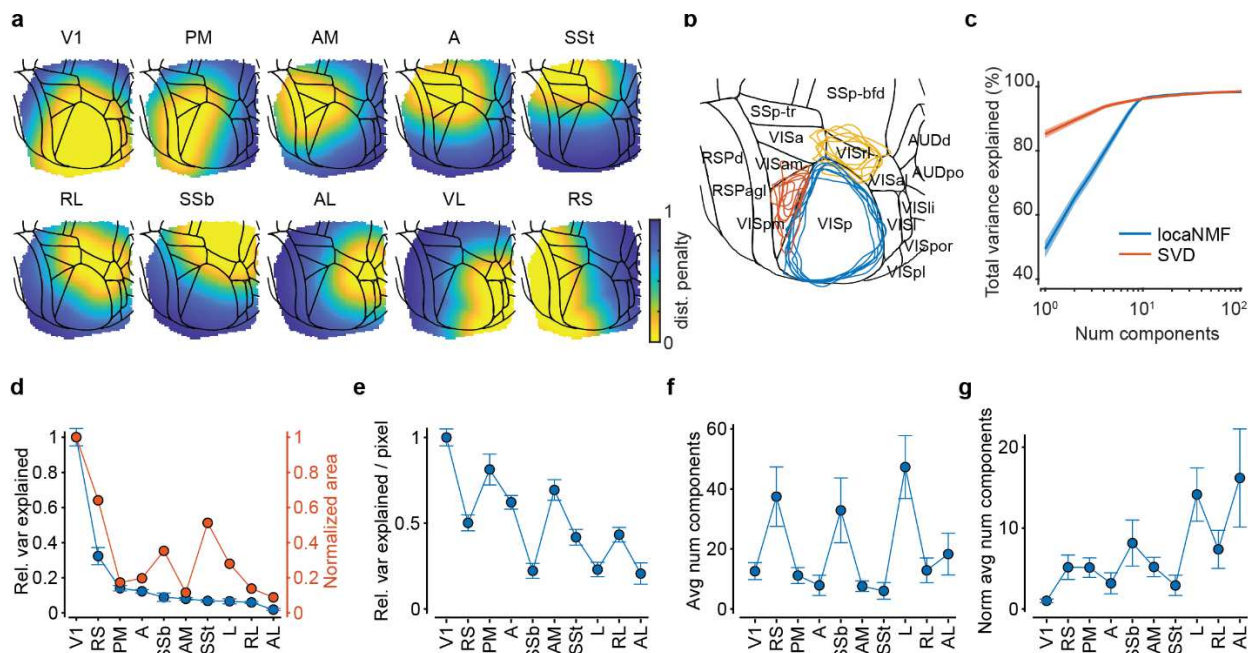


680
 681 **Figure 4 | Choice is distributed, near orthogonal to other components and with a ventral-stream**
 682 **dominance.** **a**, Spatial-Distribution index (SDI,) for each state vector. Choice had the largest SDI ($30 \pm$
 683 4%); dots are different animals; middle lines and shaded areas are means and 95% CI. **b**, Angles
 684 between state vectors. Choice axes (pre- and post-movement) were orthogonal to all other axes
 685 (smallest angle $84 \pm 7^\circ$). Attention and wheel had the smallest angular separation ($44 \pm 3^\circ$), followed by
 686 wheel and saccades ($56 \pm 4^\circ$). **c**, Pairwise correlations between the d' indices obtained from each area
 687 used for hierarchical clustering. **d**, Hierarchical clustering from the pairwise correlations shown in **c**.
 688 Attention and wheel movements were most similar, followed by saccades. Choice pre- and post-
 689 movement onset clustered together, whereas stimulus showed the most dissimilar pattern. **e**, We
 690 computed five d' values, each derived by restricting locaNMF components to one of the five area
 691 groups, thus defining a 5-D space for d' components. The five broad area groups consisted of the dorsal
 692 stream (PM and AM), ventral stream (L), posterior parietal (A, AL and RL), somatosensory (SSt and SSb)
 693 and retrosplenial (RS) regions.

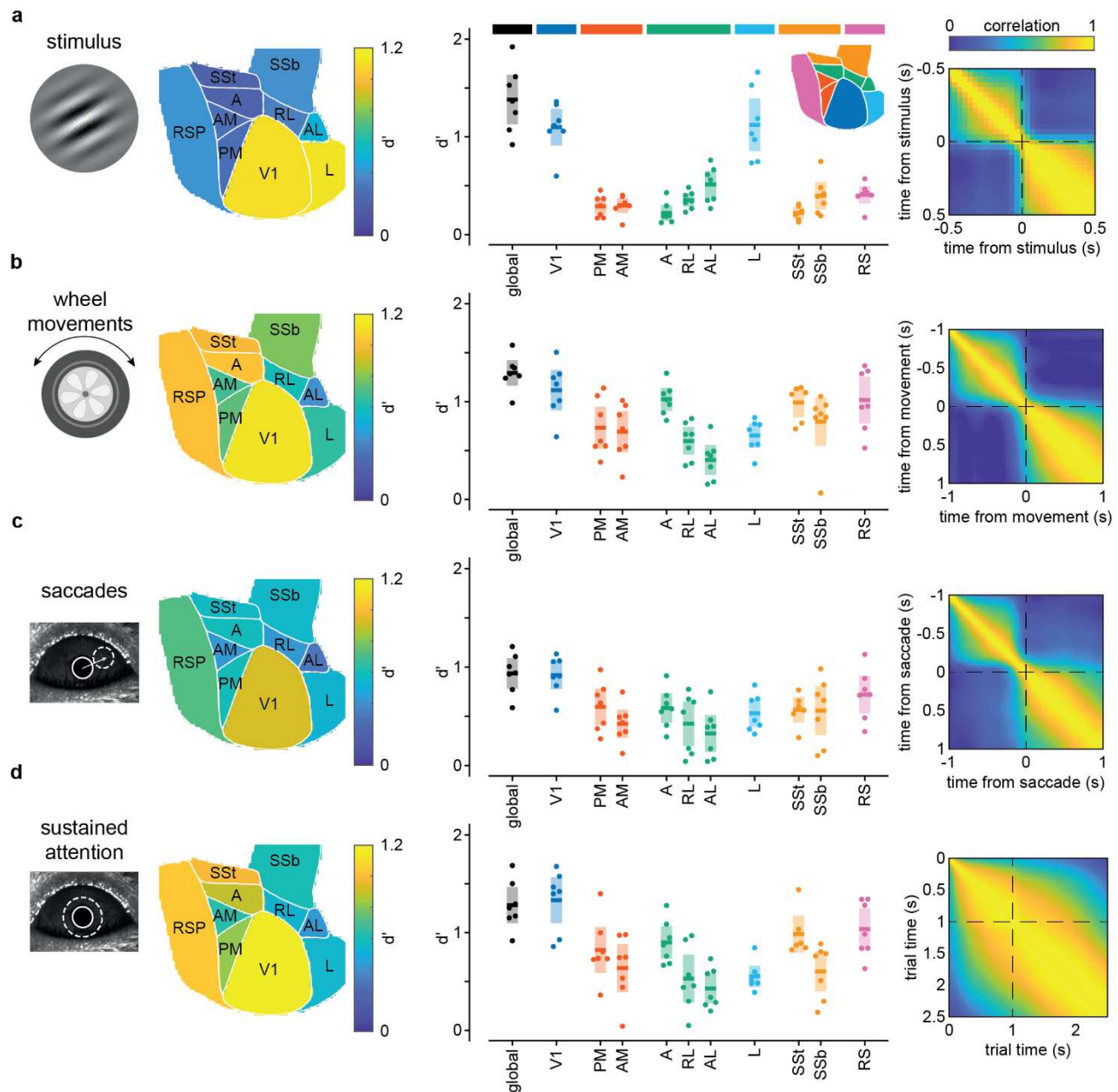


694 **Figure 5 | RNN model relates neural representations to DM computations.** **a**, Left: recurrent neural
695 network (RNN) architecture consisting of a module with $N = 128$ recurrently connected units. The
696 module receives two inputs for the left and right stimuli, and one input for the attentional state. It
697 generates a continuous output that will determine the choice. Right: Psychometric curves used to
698 determine the proportion of L/R-choice trials in the training set for each difficulty level, depending on
699 the attention state. **b**, Psychometric curves from the trained model showing that the model generalizes
700 to intermediate values of attention and difficulty. **c**, Projection of L/R easy and hard trials onto the
701 choice axis (state vector) following the same methods used in Fig. 2. Shaded bar denotes the selected
702 time used for state vector averaging. **d**, The choice axis became stable quickly after the stimulus
703 presentation ($t = 1$ s). **e**, State vectors for choice, computed separately in each trial based on difficulty
704 level, were almost parallel to each other, with the largest deviation staying below 20° . **f**, Discriminability
705 for choice (d') was higher in easy trials than in hard trials. Line and shaded area are the mean and 95% CI
706 across 10 trained networks with different random initializations. **g**, Choice was modulated by attention,
707 as shown by the increase in discriminability values in trials with high attention levels. **h**, Diagram of the
708 projected trajectories in the space spanned by the axes of choice and attention.

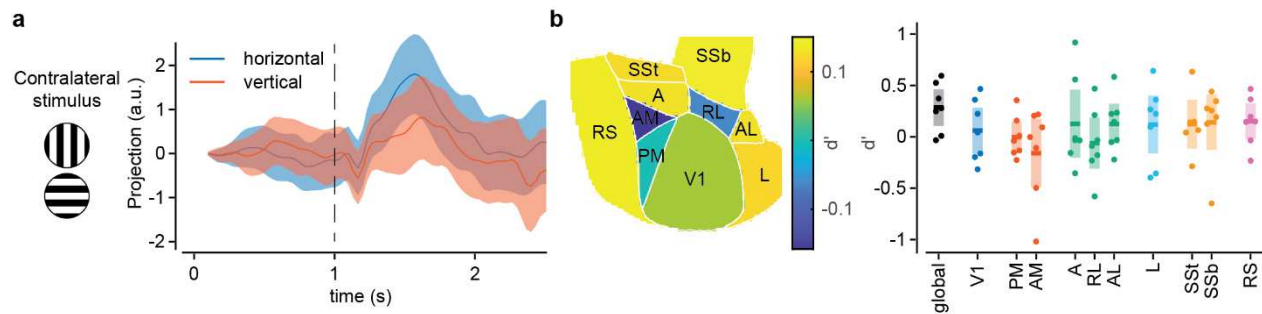
Extended Data Figures



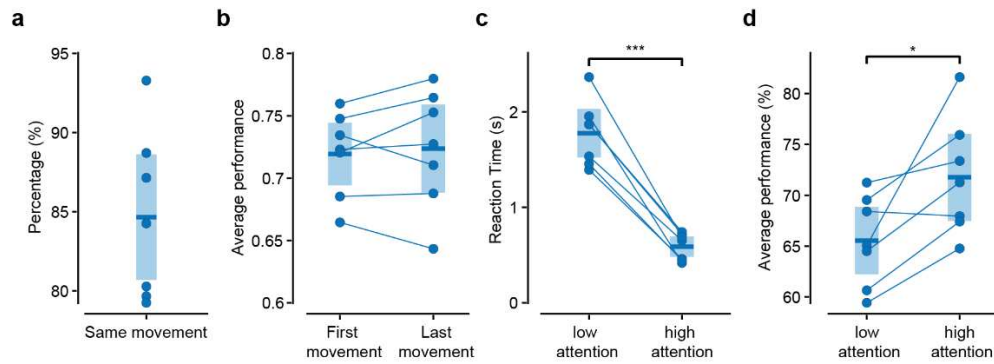
709 **Extended Data Figure 1 | Statistics of locaNMF decomposition.** **a**, Pixel-wise distance penalty maps
 710 used to initialize the ten regions for the locaNMF decomposition. Penalties within the boundaries of
 711 each region were 0 and increased exponentially with distance from the boundary. **b**, Superposition of
 712 retinotopically aligned animals (blue, red, and yellow contours) with the Allen Brain Atlas. **c**, Total
 713 variance explained as a function of the number of components for locaNMF and standard singular-value
 714 decomposition (SVD) for a given animal. **d**, Blue = relative variance explained with respect to V1 for each
 715 of the areas ordered by their variance explained. Red = surface areas relative to V1. **e**, Fraction of the
 716 total variance explained by the locaNMF components from each region normalized by the number of
 717 pixels in each region. **f**, Number of components required in each area to reach 99% of total EV, averaged
 718 across animals. This number does not simply reflect area sizes; for instance, L decomposition resulted in
 719 many components in all animals despite being a small region. **g**, Average number of components as in **f**,
 720 normalized by the size of each region.



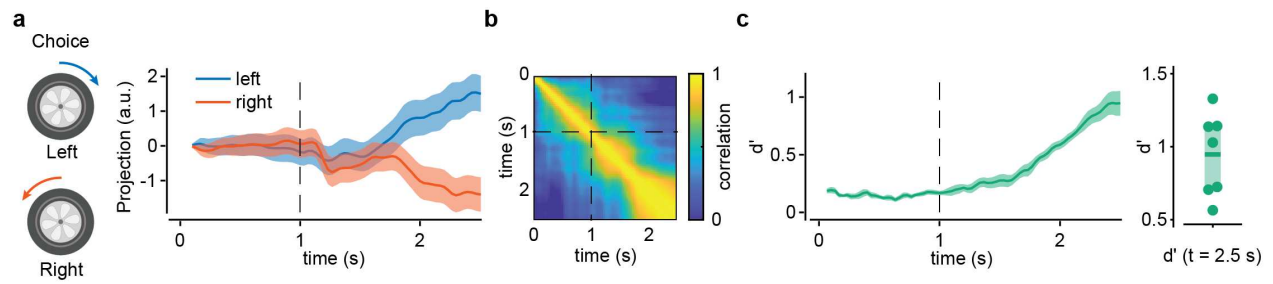
721 **Extended Data Figure 2 | Sensory, movement and top-down discriminability statistics across areas. a,**
 722 Average discriminability d' for each area for stimulus, wheel movements, saccades, and sustained
 723 attention (top to bottom rows). **b,** Statistics for global d' values (ignoring source location), and for each
 724 individual area across animals. Individual dots for each animal, middle bar is the mean, and shaded area
 725 is 95% CI of the mean. Inset: color-code reference for each of the areas. **c,** Stability of each global state
 726 vector in time for a representative animal. For stimulus, wheel movements, and saccades, the state
 727 vector becomes stable immediately after the event onset, whereas for sustained attention it is stable
 728 throughout the trial.



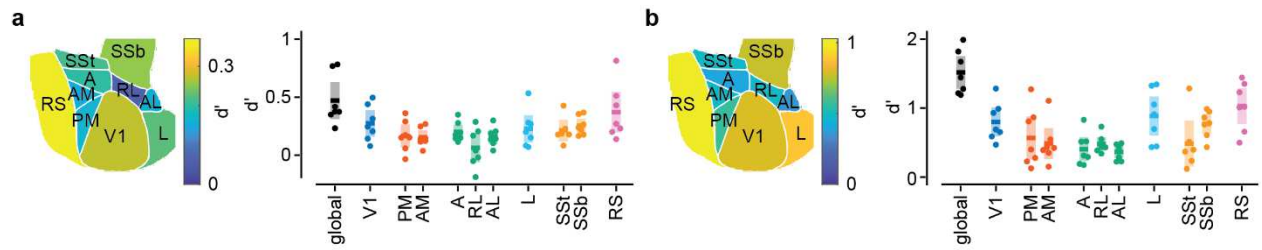
729 **Extended Data Figure 3 | Widefield activity contained no information about the contralateral stimulus**
 730 **orientation.** **a**, Time dependence of response projections onto a state vector defined using horizontal or
 731 vertical contralateral stimulus trials for a representative animal. Trajectories did not split during the trial.
 732 The line is the trial average, and shaded areas are s.e. **b**, Statistics for global and area-specific d' for the
 733 same state-vector. All area-based d' values were consistent with no discriminability power; each dot is
 734 one animal, middle bar and shaded area are the average across animals and 95 % CI.



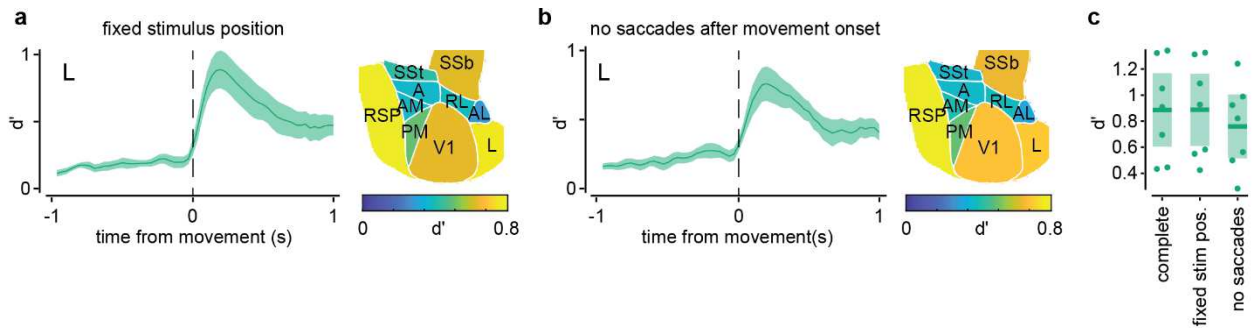
735 **Extended Data Figure 4 | First-movement correlation with choice and attention-dependent**
 736 **performance.** **a**, Fraction of occurrences when the direction of the first wheel movement coincided with
 737 the direction of the last movement in the trial (i.e., the movement that ended the trial). **b**, Comparison
 738 of overall performance when considering either the first or the last movement (paired t-test, $p = 0.8$). **c**,
 739 Reaction times for the first movement depended on attention, being significantly shorter in high
 740 attention trials (paired t-test, $p = 4 \cdot 10^{-5}$). **d**, Average performance was consistently higher in high-
 741 attention trials (paired t-test, $p = 0.02$). In all panels, a dot indicates one animal; the middle bar and
 742 shaded area are the average across animals and 95 % CI.



743 **Extended Data Figure 5 | Choice signals can be distinguished in trial time.** **a**, Projections onto the state
 744 vector for choice defined according to trial-time—not movement time— for a representative animal.
 745 Only trials in which the first movement appeared in the 1.5 to 2.5 s window were included. Trajectories
 746 started to split within the same window **b**, Stability of the choice state vector in trial time. A first
 747 signature of stability appears soon after stimulus onset. **c**, Global d' evolution for the same state vector
 748 averaged across animals (left), and statistics of peak values (right; each dot is one animal, middle bar
 749 and shaded area are the average across animals and 95% CI). D' starts to increase immediately after
 750 stimulus onset and before movement onset.



751 **Extended Data Figure 6 | Choice-specific area contributions.** **a** and **b**, Global and area-based d' statistics
 752 for the choice state vector according to movement time (Figure 3 main text); before movement onset
 753 (left, $t = -0.1$ s), and peak values after movement onset (right, $t = 0.3$ s).



755 **Extended Data Figure 7 | Ventral stream choice signature is not linked to eye or stimulus movements.**

756 **a**, Left: Evolution of choice d' for area L during trials where the first movement occurred within 1 s of the
 757 stimulus presentation, i.e., the stimulus was always in the same position on the screen. Right: area-
 758 specific d' 0.2 s after movement for the same trials. **b**, As in **a**, but also with the constraint that there
 759 were no saccades 0.5 s before or after the movement onset. **c**, Comparison of peak d' values in area L
 760 for the three controlled conditions: complete (same as Fig. 3 on the main text), and those shown here in
 761 panels **a** and **b**.

Figures

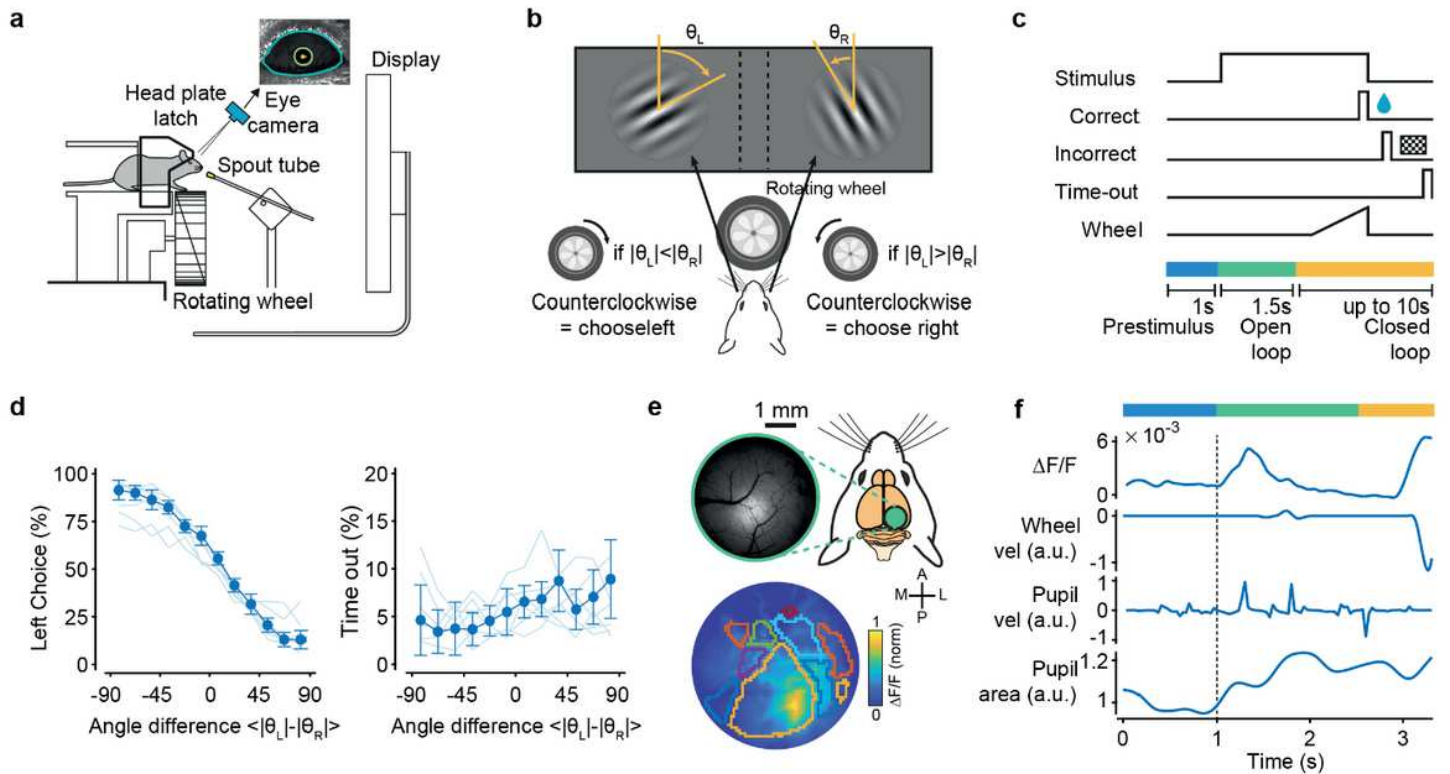


Figure 1

Imaging dorsal-parietal areas during an orientation discrimination task. **a**, Mice were trained on a 2AFC orientation discrimination task using an automated setup featuring voluntary head fixation. They signaled a L/R choice by rotating a toy wheel with their front paws. **b**, Mice rotated the wheel to position the most vertical of two oriented gratings in the center of the screen. **c**, Trial structure: After a 1 s pre-stimulus period, the stimulus was presented, followed by a 1.5 s OL interval in which wheel movements were decoupled from stimulus movements. Thereafter, in the CL period, wheel rotations resulted in L/R horizontal shifts of the stimuli. Correct choices were rewarded with water; incorrect choices were followed by a checkerboard pattern presentation. Ten seconds of no movement in the CL period triggered a time-out period. **d**, Left: mice's performance in the task (fraction of left choices) as a function of angle difference from the target orientation (nominal value of zero). Thick line = mean (\pm s.e.) across animals; thin lines = individual animals. Right: fraction of timeout trials as a function of difficulty. Timeout trials did not depend on task difficulty. **e**, Widefield calcium imaging of the posterior cortices of Thy1-GCaMP6f mice, with retinotopic mapping of 10–12 visual areas (colored contours). **f**, Simultaneously recorded fluorescence signals (dF/F), wheel and eye velocities, and pupil areas. In this example, choice was signaled at $t = 3.1$ s (by a sharp increase in wheel velocity).

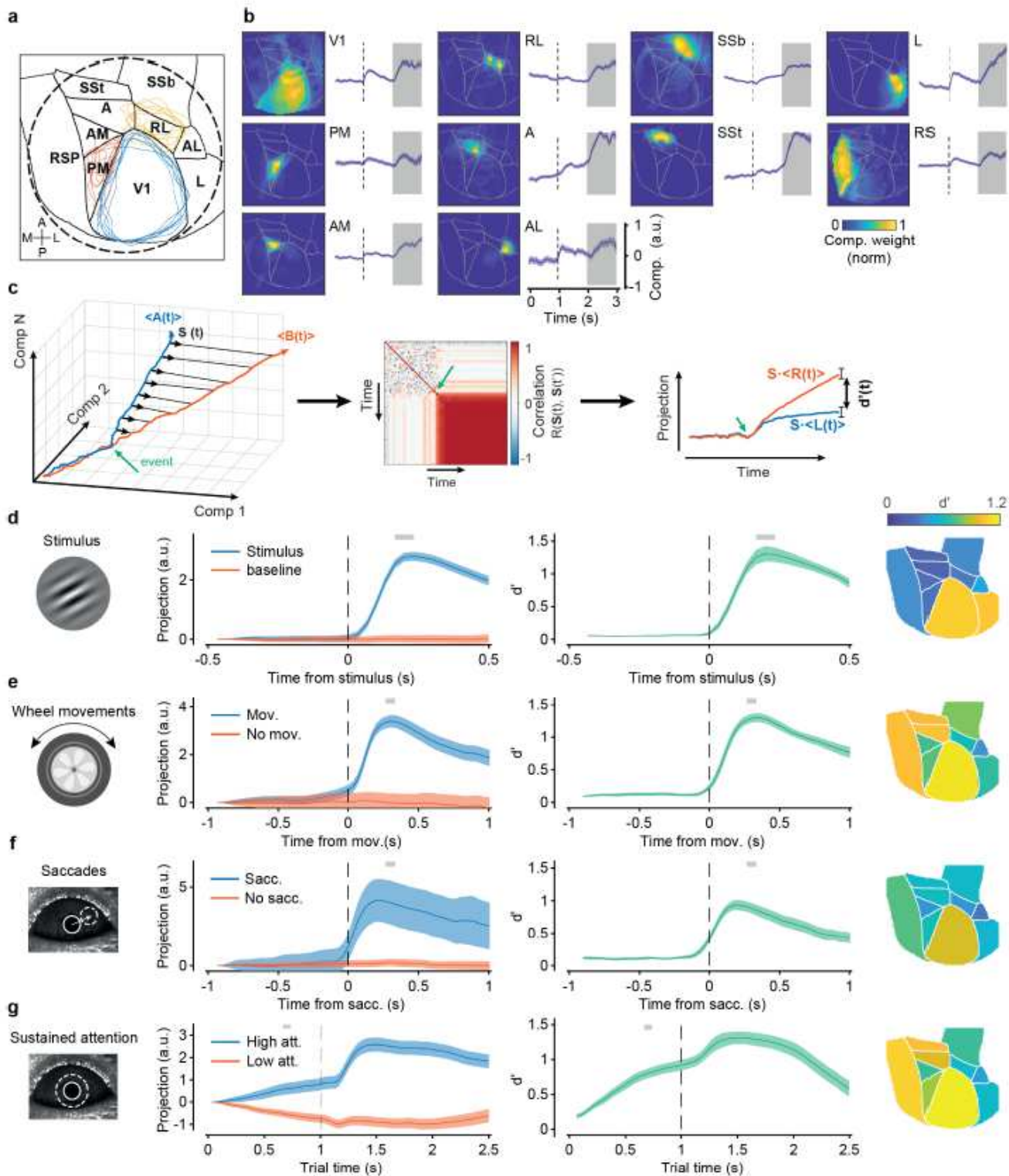


Figure 2

LocaNMF decomposition identifies sensory, behavioral, and attention-related variables. **a**, Characteristic imaging window (dashed circle) superimposed on 10 cortical areas from the Allen Brain Atlas reference framework. Blue, red, and yellow contours are the reference-aligned area boundaries for V1, PM and RL for each animal. **b**, Spatial weights and trial-averaged time-series of the largest locaNMF components for each of the 10 seeding regions (Extended Data Fig. 1) for a representative animal. Selected trials for the

trial-average all presented wheel movements within the 1 s shaded region. c, Schematic for the definition of state vectors. The direction of the state vector becomes stable after an event indicated by the green arrow. Vector stability is measured as the temporal autocorrelation $r(S(t), S(t'))$, (right panel). Projections (cross-validated) of the two variables $A(t)$ and $B(t)$ onto S separately over time, as quantified by a d' discriminability measure. d, Stimulus-related state vector. Left: projections of trials with and without a stimulus response onto the stimulus state vector for a given animal. Lines and shaded regions indicate projection averages across trials and s.e. Middle: Discriminability d' over time, averaged across all animals. Gray bars on top, epoch used for the time-average of the state vector. Right: area-specific peak d' scores obtained by defining the state vector using only the components originating from that area. e, As in d, but aligned to movement-detection time, i.e., separability between trials with and without a detected wheel movement. f, As in e, but for saccadic eye movements. g, As in f, but for sustained attention. High- and low-attention trials were defined based on pupil area changes, using the highest or lowest 33rd percentile of the area-change distribution.

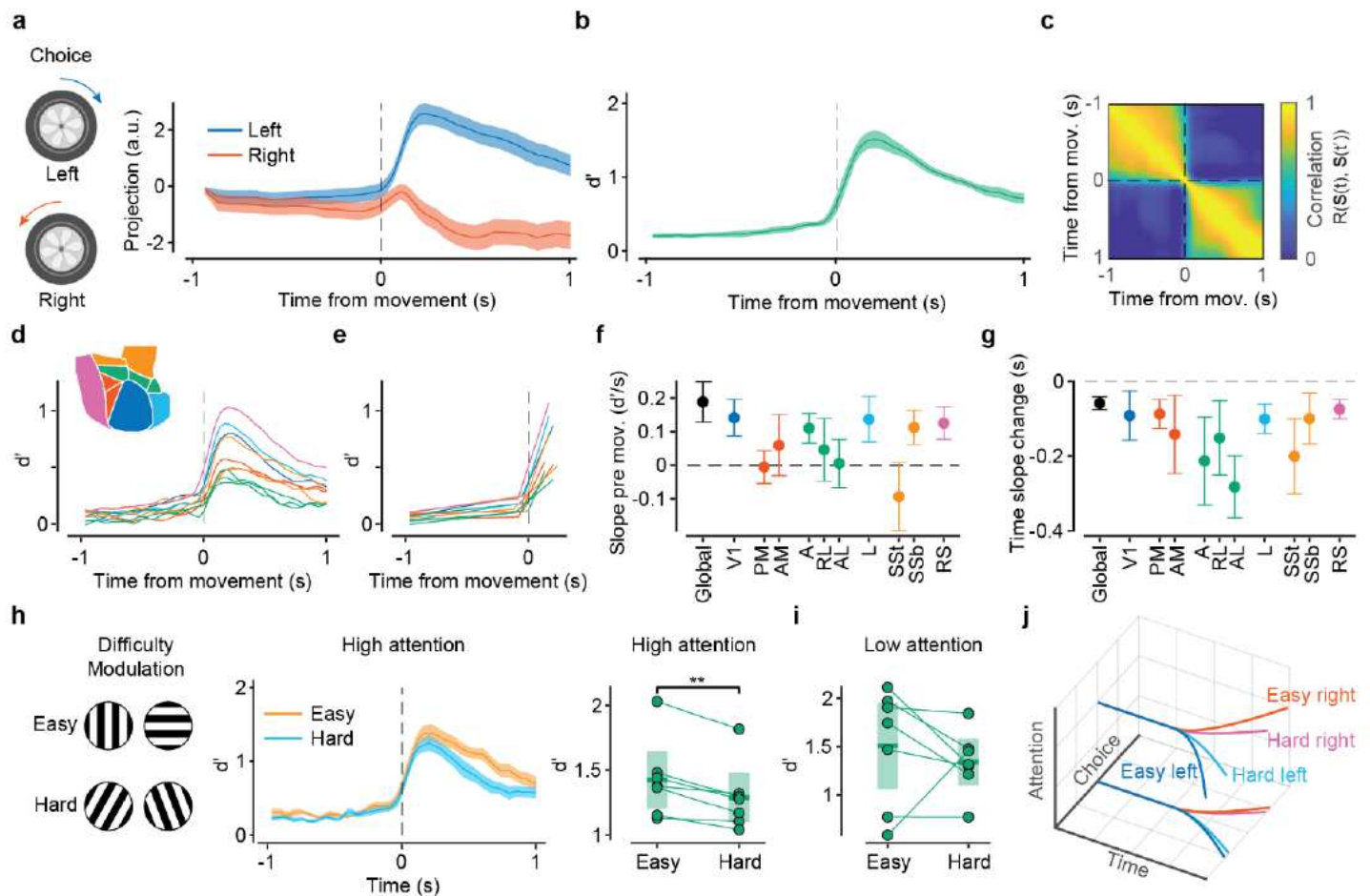


Figure 3

Choice signals have pre-motor component and are modulated by task difficulty and attentions. a, Projections on the state vector for choice signals for a characteristic animal (line for trial average and shaded area for s.e.). Wheel movements signaling either a left or a right choice were aligned to the wheel movement onset. b, Evolution of d' discriminability relative to movement time averaged across animals.

Early and late choice periods were defined relative to movement onset. c, Temporal stability of the state vector for choice. There is a clear change in the contribution of the choice state vector near the time of movement onset. Same animal as in a. d, Temporal evolution of area-specific d' curves (inset: area color code). e, Piecewise linear fits of the curves in d in pre- and post-movement periods. f, Pre-movement slopes fitted in e for different areas; error bars, 95% confidence intervals (CI) across animals. g, Times of slope change for different areas from the fits in e. Data and colors as in f. h, Left: evolution of choice discriminability, d' , in high attention states for easy and hard trials (angle difference $>$ or $<$ 45°). Right: Paired comparisons of peak d' values for each animal ($p = 0.003$). i, As in h, but for low-attention states. Paired differences were not significant ($p = 0.50$). j, Schematic representation of the temporal evolution of left and right trajectories with difficulty and attention.

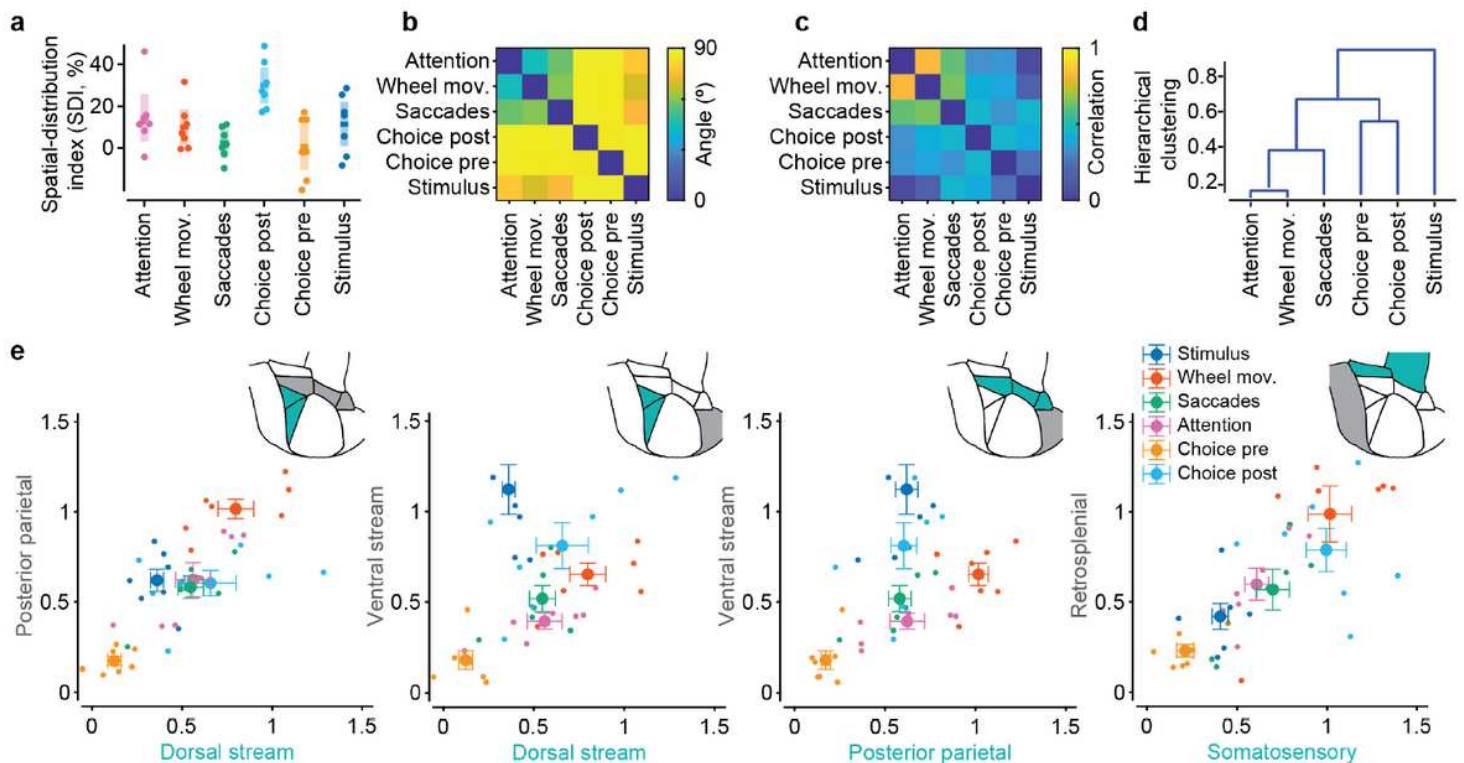


Figure 4

Choice is distributed, near orthogonal to other components and with a ventral-stream dominance. a, Spatial-Distribution index (SDI) for each state vector. Choice had the largest SDI ($30 \pm 4\%$); dots are different animals; middle lines and shaded areas are means and 95% CI. b, Angles between state vectors. Choice axes (pre- and post-movement) were orthogonal to all other axes (smallest angle $84 \pm 7^\circ$). Attention and wheel had the smallest angular separation ($44 \pm 3^\circ$), followed by wheel and saccades ($56 \pm 4^\circ$). c, Pairwise correlations between the d' indices obtained from each area used for hierarchical clustering. d, Hierarchical clustering from the pairwise correlations shown in c. Attention and wheel movements were most similar, followed by saccades. Choice pre- and post-movement onset clustered together, whereas stimulus showed the most dissimilar pattern. e, We computed five d' values, each derived by restricting locaNMF components to one of the five area groups, thus defining a 5-D space for d'

components. The five broad area groups consisted of the dorsal stream (PM and AM), ventral stream (L), posterior parietal (A, AL and RL), somatosensory (SSt and SSb) and retrosplenial (RS) regions.

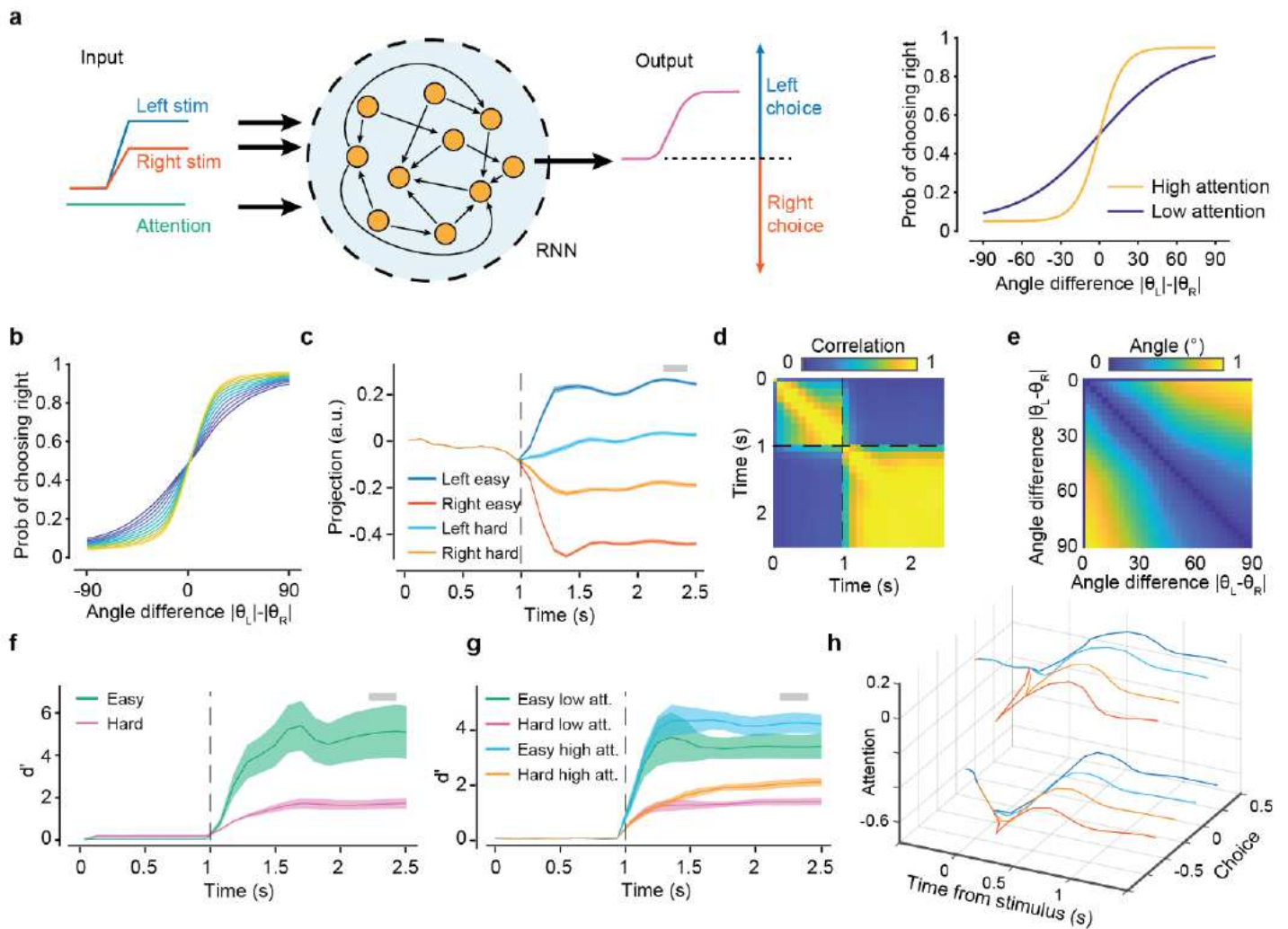


Figure 5

RNN model relates neural representations to DM computations. **a**, Left: recurrent neural network (RNN) architecture consisting of a module with $N = 128$ recurrently connected units. The module receives two inputs for the left and right stimuli, and one input for the attentional state. It generates a continuous output that will determine the choice. Right: Psychometric curves used to determine the proportion of L/R-choice trials in the training set for each difficulty level, depending on the attention state. **b**, Psychometric curves from the trained model showing that the model generalizes to intermediate values of attention and difficulty. **c**, Projection of L/R easy and hard trials onto the choice axis (state vector) following the same methods used in Fig. 2. Shaded bar denotes the selected time used for state vector averaging. **d**, The choice axis became stable quickly after the stimulus presentation ($t = 1$ s). **e**, State vectors for choice, computed separately in each trial based on difficulty level, were almost parallel to each other, with the largest deviation staying below 20° . **f**, Discriminability for choice (d') was higher in easy trials than in hard trials. Line and shaded area are the mean and 95% CI across 10 trained networks with different

random initializations. g, Choice was modulated by attention, as shown by the increase in discriminability values in trials with high attention levels. h, Diagram of the projected trajectories in the space spanned by the axes of choice and attention.